

**MICROSTRUCTURAL INVESTIGATION OF THE EFFECT OF Cr ON  
 $\gamma'$  PRECIPITATION DURING SOLUTIONIZATION IN Co/Ni BASED  
SUPERALLOY**

Submitted in partial fulfilment of the requirements of the degree of

**MASTER OF TECHNOLOGY  
(MATERIALS TECHNOLOGY)**

Submitted by,

**Mr. Aloysius Lobo  
(Roll No 205602)**

Under the guidance of

**Dr. Bonta Srinivasa Rao  
Assistant Professor**

**M. Ramakrishna  
Scientist – E**



**DEPARTMENT OF METALLURGICAL AND MATERIALS  
ENGINEERING**

**NATIONAL INSTITUTE OF TECHNOLOGY  
WARANGAL**

**June, 2022**

## **APPROVAL SHEET**

This Dissertation Work entitled "**Microstructural investigation of the effect of Cr on  $\gamma'$  precipitation during solutionization in Co/Ni based superalloy**" by **Mr. Aloysius Lobo** is approved for the degree of **Master of Technology (M.Tech) in Materials Technology**

### **Examiners**

Dr. Bonta Srinivasa Rao  
Assistant Professor  
Department of Metallurgical and  
Materials Engineering (MMED)  
NIT Warangal

M. Ramakrishna  
Scientist – E  
International Advanced Research for Powder  
Metallurgy and New Materials (ARCI)  
Hyderabad

### **Chairman**

*DATE: 27 June 2022*

*PLACE: NIT WARANGAL*

## **DECLARATION**

I 'Mr. Aloysius Lobo' declare that this written submission represents my ideas in my own words and where ever others' ideas or words have been included, I have adequately cited and referenced the original source. I also declare that I have adhered to all principles of academic honesty and integrity and have not misinterpreted or fabricated or falsified any idea/data/fact/source in my submission. I understand that any violation of the above will be a cause for disciplinary action by the Institute and can also evoke penal action from the sources which have thus not been properly cited or from whom proper permission has not been taken when needed.

ALOYSIUS LOBO

ROLL NO: 205602

DATE: 27 June 2022

## **CERTIFICATE**

This is to certify that the work presented in the thesis entitled "**Microstructural investigation of the effect of Cr on  $\gamma'$  precipitation during solutionization in Co/Ni based superalloy**" is a bonafide record of work carried out by "Mr. Aloysius Lobo (Roll. No: 205602)" submitted to the faculty of "Department of Metallurgical and Materials Engineering", in partial fulfilment of the requirements for the award of the degree of Master of Technology in "Materials Technology" at National Institute of Technology, Warangal during the academic year 2020 – 2022.

Dr. Bonta Srinivasa Rao  
Assistant Professor  
Department of Metallurgical and  
Materials Engineering (MMED)  
NIT Warangal

M. Ramakrishna  
Scientist – E  
International Advanced Research for Powder  
Metallurgy and New Materials (ARCI)  
Hyderabad

## **ACKNOWLEDGMENT**

With immense pleasure, I wish to express my deep appreciation and gratitude to my supervisor Asst. Prof. Dr. Bonta Srinivasa Rao, NIT-Warangal, and Mr. M. Ramakrishna, Scientist 'E' ARCI, Hyderabad and Dr. K. Suresh, Scientist 'E' ARCI, Hyderabad for their inspiring guidance, constant encouragement, attention, and efforts throughout the course of this work. Their cheerful disposition, openness to new ideas, and warm support will be remembered at all times.

I am thankful to the Director, Dr. T. N. Rao of ARCI for giving me the permission to carry out my project work at ARCI. I also thank the Team Leader of the Centre for Materials Characterization and Testing (CMCT), Dr. G. Ravi Chandra, Scientist' F', ARCI for his continued support, encouragement, and valuable suggestions.

I would like to thank the Staff of CMCT, ARCI Hyderabad, Mrs. Chalavadi Prashanthi, Mr. G. Murthy and Mr. Janaki Rao for their technical support to assist me in carrying out the experiments and characterization. Also, sincere thanks to the Ph.D. students in ARCI as well as NIT Warangal for helping me in whichever way possible.

I would like to express my sincere thanks to my parents for supporting me to undergo this course and constantly being my backbone during critical times.

*Date: 27 June 2022*

*ALOYSIUS LOBO*

## TABLE OF CONTENTS

	Page No.
APPROVAL SHEET	II
DECLARATION	III
CERTIFICATE	IV
ACKNOWLEDGEMENTS	V
LIST OF FIGURES	IX
LIST OF TABLES	XIV
NOMENCLATURE	XV
ABSTRACT	XVI
CHAPTER 1. INTRODUCTION	1
CHAPTER 2. LITERATURE REVIEW	4
2.1 Novel Cobalt-based $\gamma/\gamma'$ Alloys	4
2.2 Low Density, High-Temperature Co-based Superalloys	6
2.2.1 Co-10Al-5Mo-2Nb at.%	7
2.2.2 Co-10Al-5Mo-2Ta at.%	7
2.2.3 Co-30Ni-10Al-5Mo-2Ta-xTi (x = 0,1,2,4 at %)	8
2.3 Coarsening of Precipitates	9
2.3.1 Factors affecting coarsening of precipitates	10
2.4 $\gamma'$ dissolution and formation of cooling precipitates	11
2.5 Effect of cooling rates on $\gamma'$ precipitation behavior	14
2.6 Effect of lattice misfit on precipitate size and morphology	18

2.7 Aging studies of Co-Ni-Al-Ti based superalloy	22
2.8 OBJECTIVES	23
2.9 PROCESS FLOW	24
<b>CHAPTER 3. EXPERIMENTAL PROCEDURE</b>	<b>25</b>
3.1 Materials	25
3.2 Alloy Preparation	26
3.2.1 Arc melting processing route	26
3.3 Heat Treatments	26
3.4 Microstructural Characterization	29
3.4.1 High Flux X-Ray Diffractometer (HF-XRD)	29
3.4.2 Inverted Optical Microscope	31
3.4.3. Field Emission Gun – Scanning Electron Microscope (FEG - SEM)	32
3.5 Mechanical Characterization	33
Vickers Microhardness Tester	33
<b>CHAPTER 4. RESULTS AND DISCUSSIONS</b>	<b>36</b>
4.1 As-cast alloys	36
4.1.1 Microstructure of as-cast alloys	36
4.1.2 EDAX -EDS Analysis	37
4.1.3 Scanning Electron Microscopic Images	39
4.2 Differential Scanning Calorimetry (DSC) Studies	40
4.3 X-Ray Diffraction Analysis	41
4.4 As-solutionized samples	43
4.4.1 Field Emission – Scanning Electron Microscope (FE-SEM)	43

4.4.1.1 Solutionization at 1150°C	43
4.4.1.2 Particle size distribution curve	44
4.4.1.3 Solutionization at 1200°C	47
4.4.1.4 Particle size distribution curve	47
4.5 Effect of cooling rates [Microstructural Analysis]	51
4.5.1 Water Quenching (WQ)	51
4.5.2 Air Cooling (AC)	52
4.5.3 Furnace Cooling (FC)	53
4.6 XRD and lattice misfit measurements	55
4.6.1 Effect of cooling rates [XRD Analysis]	56
4.7 Microhardness Measurements	60
4.8 Property relation with varying at.% Cr	62
<b>CHAPTER 5. CONCLUSIONS AND FUTURE SCOPE</b>	64
<b>REFERENCES</b>	65

## LIST OF FIGURES

---

	<b>Title</b>	<b>Page</b>
	<b>No.</b>	
Fig 2.1: (a) The average $\gamma'$ precipitate size ( $\langle r \rangle$ ) and their number density ( $N_v$ ) as a function of Ti content in the alloy (b) Variation of $\gamma/\gamma'$ lattice misfit with Ti content in the alloy for as-solutionized and after aging at 900 °C for 50h.	8	
Fig 2.2: Temporal evolution of (a) $\gamma'$ volume fraction (%), (b) Average precipitate size ( $\langle r(t) \rangle$ ) in 3Ti and 4Ti alloys during isothermal aging at 900 °C and 950 °C.	9	
Fig 2.3: Microstructures of $\gamma'$ precipitates heated at (a) 1160°C for 15 min; (b) 1160°C for 30 min; (c) 1180°C for 30 min; (d) 1180°C for 45 min; (e) 1200°C for 15 min; (f) 1200°C for 45 min.	11	
Fig 2.4: Effect of solution treatment conditions on $\gamma'$ precipitates.	12	
Fig 2.5: Variations of $\gamma-\gamma'$ lattice mismatch with heat treatment temperature and time for Rene®80.	13	
Fig 2.6: Deconvolution of the corresponding peaks to the $\gamma$ and $\gamma'$ phases	13	
Fig 2.7: DSC curves demonstrating $\gamma'$ precipitation peaks during cooling.	14	
Fig 2.8: Average diameter of $\gamma'$ precipitates as a function of cooling rate.	15	
Fig. 2.9: Influence of cooling methods on the (a) tensile, (b) elongation and (c) microhardness values of GH4169 Ni-based superalloy	16	
Fig 2.10: (a) 0.2% proof stress of Waspaloy, MAR M 247, Co-9Al-11W, Co-9Al-10W-2Ta and Haynes 188 superalloys with temperature and (b) solvus temperature		

of Co–10Al–5Mo–2Ta, Co–30Ni–10Al–5Mo–2Ta, Co–30Ni–10Al–5Mo–2Ta– 2Ti, Co–9Al–9.8W alloy, Co–35Ni–9Al–10W alloy and nickel-based superalloy (Waspaloy).	17
Fig 2.11: Collective results showing the variation of the Vickers hardness, lattice parameters of the $\gamma$ and $\gamma'$ phases and lattice misfit as a function of the concentration of Ti (in at.%) in the alloys.	18
Fig 2.12: XRD of (111) diffraction peaks of aged superalloys.	20
Fig 2.13: The mean size of secondary and tertiary $\gamma'$ particles as a function of cooling rates shows an approximately linear relationship in the log-log plot.	21
Fig 2.14: Variation of (a) Vickers Hardness and (b) tensile and yield strength as a function of lattice misfit.	22
Fig. 3.1: Vacuum Arc Melting Furnace (VEC Solutions)	26
Fig 3.2: Netzsch STA 449 F3 Jupiter make Differential Scanning Calorimetry (DSC).	27
Fig 3.3: Homogenization heat treatment of 4 alloy systems done in (a) VBCC Box furnace at 1200°C and (b) Indfurr Muffle Furnace at 1150°C	27
Fig 3.4: Heat-treatment cycle	28
Fig 3.5: Showing samples enclosed in vacuum-sealed quartz tubes.	28
Fig 3.6: Showing the schematic of the rotating anode of the HF-XRD generator.	29
Fig 3.7: Rigaku SmartLab HF-XRD generator.	30
Fig 3.8: Olympus Inverted Optical Microscope.	31
Fig 3.9: Zeiss GeminiSEM500 FEG-SEM	32

Fig 3.10: UHL VHMT Vickers Microhardness Tester.	33
Fig. 4.1: Inverted Optical images of as-cast alloys (a) A1-0 at.%Cr, (b) A2-10 at.%Cr, (c) A3-20 at.%Cr.	36
Fig. 4.2: Line scan of as-cast alloys (a) A1-0 at.%Cr, (b) A2-10 at.%Cr, (c) A3-20 at.%Cr	38
Fig. 4.3: SEM images of as-cast alloys (a) A1-0 at.%Cr, (b) A2-10 at.%Cr and (c) A3-20 at.%Cr.	39
Fig. 4.4: DSC results of as-cast alloys A1-0 at.%Cr, A2-10 at.%Cr and A3-20 at.%Cr.	40
Fig. 4.5: ThermoCalc results of as-cast alloys (a) A1-0 at.%Cr, (b) A2-10 at.%Cr and (c) A3-20 at.%Cr.	41
Fig. 4.6: XRD plots of as-cast alloys (a) A1-0 at.%Cr, (b) A2-10 at.%Cr and (c) A3-20 at.%Cr showing FCC crystal structure.	42
Fig. 4.7: SEM images of $\gamma/\gamma'$ microstructure of alloys heat treated at 1150°C followed by (a)-(c) WQ, (d)-(f) AC, (g)-(i) FC; (a)-(g) 0at.% Cr, (b)-(h) 10at.% Cr, (c)-(i) 20at.% Cr.	43
Fig. 4.8: Histograms showing a unimodal size distribution of $\gamma'$ for the alloys (a) 0at.% Cr, (b) 10at.% Cr, (c) 20at.% Cr heat-treated at 1150°C and AC	44
Fig. 4.9: Histograms showing a bimodal size distribution of $\gamma'$ for the alloys (a) 0at.% Cr, (b) 10at.% Cr, (c) 20at.% Cr heat-treated at 1150°C and FC	46
Fig. 4.10: SEM images of $\gamma/\gamma'$ microstructure of alloys heat treated at 1200°C followed by (a)-(c) WQ, (d)-(f) AC, (g)-(i) FC; (a)-(g) 0at.% Cr, (b)-(h) 10at.% Cr, (c)-(i) 20at.% Cr.	47

Fig. 4.11: Histograms showing a bimodal size distribution of $\gamma'$ for the alloys (a) 0at.% Cr, (b) 10at.% Cr, (c) 20at.% Cr heat-treated at 1200°C and AC	48
Fig. 4.12: Histograms showing a bimodal size distribution of $\gamma'$ for the alloys (a) 0at.% Cr, (b) 10at.% Cr, (c) 20at.% Cr heat-treated at 1200°C and FC.	49
Fig. 4.13: SEM micrographs of alloys (a) 0at.% Cr, (b) 10at.% Cr and (c) 20at.% Cr heat treated at 1150°C while (d) 0at.% Cr, (e) 10at.% Cr and (f) 20at.% Cr heat-treated at 1200°C followed by WQ.	51
Fig. 4.14: SEM micrographs of alloys (a) 0at.% Cr, (b) 10at.% Cr and (c) 20at.% Cr heat treated at 1150°C while (d) 0at.% Cr, (e) 10at.% Cr and (f) 20at.% Cr heat-treated at 1200°C followed by AC.	52
Fig. 4.15: SEM micrographs of alloys (a) 0at.% Cr, (b) 10at.% Cr and (c) 20at.% Cr heat treated at 1150°C while (d) 0at.% Cr, (e) 10at.% Cr and (f) 20at.% Cr heat-treated at 1200°C followed by FC.	53
Fig. 4.16: XRD plot of samples heat-treated at (a) 1150°C - WQ and (b) 1200°C - WQ.	55
Fig. 4.17: XRD plot of samples heat-treated at (a) 1150°C - AC and (b) 1200°C - AC.	55
Fig. 4.18: XRD plot of samples heat-treated at (a) 1150°C - FC and (b) 1200°C - FC.	55
Fig. 4.19: XRD (200) deconvoluted peaks for WQ samples heat-treated at (a) 10Cr, 1150°C (b) 20Cr, 1150°C (c) 10Cr, 1200°C and (d) 20Cr, 1200°C.	56
Fig. 4.20: XRD (200) deconvoluted peaks for AC samples heat-treated at (a) 0Cr, 1150°C (b) 10Cr, 1150°C (c) 20Cr, 1150°C, (d) 0Cr, 1200°C, (e) 10Cr, 1200°C and (f) 20Cr, 1200°C.	57

Fig. 4.21: XRD (200) deconvoluted peaks for FC samples heat-treated at (a) 0Cr, 1150°C (b) 10Cr, 1150°C (c) 20Cr, 1150°C, (d) 0Cr, 1200°C, (e) 10Cr, 1200°C and (f) 20Cr, 1200°C.	58
Fig. 4.22: Micro-hardness results of solutionized samples at (a) 1150°C and (b) 1200°C and (c) as-cast samples with increasing Cr content.	60
Fig. 4.23: Comparison of lattice misfit post solutionization at (a) 1150°C and (b) 1200°C with the hardness values post solutionization at (c) 1150°C and (d) 1200°C.	61
Fig. 4.24: Property relation of hardness, $\gamma'$ volume fraction and $\gamma'$ precipitate size wrt %Cr for alloys solutionized at (a) 1150°C, WQ, (b) 1200°C, WQ, (c) 1150°C, AC and (d) 1200°C, AC.	62

## LIST OF TABLES

---

<b>Title</b>	<b>Page No.</b>
Table 2.1: Nominal physical properties of Ni and Co superalloys.	4
Table 2.2: Role of alloying elements in superalloys.	5
Table 2.3: The lattice misfit, hardness and $\gamma'$ -precipitate sizes of (i) Co-27.2Ni- 3.1Al-8.1Ti-10.9Cr, (ii) Co-18.3Ni-3Al-7.8Ti-16.2Cr (iii) Co-17.3Ni-3.1Al-7.9Ti-21.5Cr.	19
Table 2.4: Showing the comparison of various Co-based and Ni-based superalloys based on $\gamma'$ solvus temperatures and hardness values after aging treatment.	23
Table 3.1: Weight measurements of alloys used for the study in at% and wt%.	25
Table 4.1: EDS elemental composition (in at.%) of the bulk material and in dendritic (D) and inter-dendritic regions (ID) of as-cast alloys A1-0 at.%Cr, A2-10 at.%Cr, A3-20 at.%Cr	36
Table 4.2: The lattice misfit for all three solutionized alloys under various cooling mediums.	58

## NOMENCLATURE

<b>WQ</b>	Water Quenched
<b>AC</b>	Air Cooled
<b>FC</b>	Furnace Cooled
<b>VAM</b>	Vacuum Arc Melting
<b>XRD</b>	X-Ray Diffractometer
<b>HF-XRD</b>	High Flux Xray Diffraction
<b>OM</b>	Optical Microscope
<b>FEG-SEM</b>	Field Emission Gun – Scanning Electron Microscope
<b>SEM</b>	Scanning Electron Microscope
<b>TCP</b>	Topologically Close Packed
<b>LSW</b>	Lifshitz-Slyozov and Wagner
<b>FWHM</b>	Full Width Half Maxima
<b>EDAX</b>	Energy Dispersive Xray Analysis
<b>EDS</b>	Energy Dispersive Spectroscopy
<b>FCC</b>	Face Centered Cubic
<b>SAXS</b>	Small Angle Xray Scattering
<b>APT</b>	Atom Probe Tomography

## ABSTRACT

The effect of the cooling rates during solutionization heat-treatment on the microstructure of age-hardenable Co-Ni-Al-Ti based superalloy is studied. The alloy is a  $\gamma/\gamma'$  age-hardenable superalloy containing cuboidal  $\gamma'$  - L1<sub>2</sub> ordered precipitates.  $\gamma'$  being the main strengthening phase in these superalloys, its evolution during heat treatment is also studied, considering its morphology and solvus temperature. Also, the effect of alloying Cr in the base alloy with varying %Cr as 0at.% Cr, 10at.% Cr and 20at.% Cr have been evaluated in this present work, and it was found that cuboidal  $\gamma'$  with sharp corners was changed to rounded cubes with increased Cr content. This is because of a decrease in the lattice misfit between  $\gamma$  and  $\gamma'$  since Cr has more affinity towards the  $\gamma$  phase and an attendant increase in the lattice parameter. Differential Scanning Calorimetric (DSC) results show that the  $\gamma'$  solvus temperature was unchanged from the 1103°C with varying Cr content.

The alloys were also investigated for the morphological changes occurring in  $\gamma'$  with varying cooling rates as cooled from the solution temperature. It was found that for higher cooling rates like air cooling (AC) and water quenching (WQ), all the alloys showed a unimodal size distribution with particle sizes less than 50nm. In contrast, bimodal size distribution with increased particle size was observed for a slower cooling rate like furnace cooling (FC). The average particle size calculated from the SEM images through ImageJ software ranged from 27nm to 37nm for the air-cooled alloys, whereas a bimodal distribution of particle size ranging from 63nm to 113nm for primary  $\gamma'$  and from 19nm to 27nm for secondary  $\gamma'$  was found for the alloys furnace cooled after heat-treating at 1150°C. Similarly,  $\gamma'$  size calculated for the alloys cooled from 1200°C under AC ranged from 16nm to 37nm while a bimodal size distribution was observed with the primary  $\gamma'$  size ranging from 179nm to 243nm and from 16nm to 29nm for secondary  $\gamma'$ .

A decrease in the lattice mismatch between  $\gamma$  and  $\gamma'$  is observed for alloys with increasing Cr content irrespective of the heat-treatment method. The lattice mismatch measured from the

deviation in d-spacing of  $\gamma$  and  $\gamma'$  phase, measured along the (200) plane, gives positive misfit values beneficial for high creep resistance at high temperatures.

# CHAPTER 1

## INTRODUCTION

Due to their use in aviation engines and other high-temperature components, nickel- and cobalt-based superalloys are typically regarded as high-temperature materials. The main strengthening factor in these superalloys is the L1<sub>2</sub> ordered  $\gamma'$  precipitates in Co/Ni FCC-  $\gamma$  matrix. However, Co-based superalloys can be proved better than Ni-based ones in various aspects like; Co has a 50°C higher melting point than Ni, which provides stability to Co-based alloys at higher temperatures. Compared to Ni, they have better corrosion properties and a stronger thermal fatigue resistance. They are resistant to the eutectic combinations with low melting points, such as Ni-Ni<sub>3</sub>S<sub>2</sub>, which crystallize at 635°C.

Co-based superalloys are usually strengthened by either solid solution strengthening or carbide strengthening. As Ni-based superalloys, Co-superalloys do not form a stable  $\gamma'$  precipitate. Some reports have reported that the  $\text{Co}_3\text{Al}$  precipitate formed in the Co-Al binary system loses its stability at temperatures greater than 873K [1]. Due to the unstable  $\text{Co}_3\text{Al}$  formation, Co-based superalloys have never achieved strengthening by age-hardening. Not until 2006, when Sato et al. discovered that by alloying W to Co-Al binary system, an L12 ordered phase can be formed, stable up to 990°C [1].  $\gamma'$  forming elements like Al, Ti, Ta, Nb, and Mo can stabilize the  $\gamma'$  phase with a solvus temperature of ~1373K. Lattice parameter mismatch, the volume fraction of the precipitates, and precipitate size are essential for strengthening the superalloy. The volume fraction of the  $\gamma'$  phase is increased by adding various  $\gamma'$  forming elements, which also aids in increasing the  $\gamma'$  solvus temperature.

Based on the lever rule, the  $\gamma'$  volume fraction can be estimated from the measured compositions of the  $\gamma$  matrix and  $\gamma'$  precipitate phases.[2]

As per the lever rule,

$$C_i^i \cdot \phi_i + C_i^i \cdot (1 - \phi_i) = C_{\text{bulk}}^i \dots \quad (1)$$

where  $\phi_i$  is the mole fraction,  $C_{\gamma'}^i$  and  $C_{\gamma}^i$  are the compositions of element i in the  $\gamma'$  precipitate and  $\gamma$  matrix phase, and  $C_{\text{bulk}}^i$  is the composition of element i in the alloy. Thus, rearranging the terms, this equation can be re-written as [2]

$$(C_{\gamma'}^i - C_\gamma^i)\phi_{\gamma'} = C_{\text{bulk}}^i - C_\gamma^i \dots \quad (2)$$

The value of lattice mismatch between  $\gamma$  and  $\gamma'$  should be less than 0.5% to maintain coherency between the precipitate and the matrix phase. It provides interfacial boundary stability, blocking the growth of  $\gamma'$  size. Coherency strengthening is also a significant contributor to yield strength. Hence, researchers try to reduce the lattice mismatch and improve the coherency. Precipitate size and shape also play a significant role in maintaining coherency and providing high-temperature strength to the alloy. [3]

Dissolution studies of newly developed high-temperature  $\gamma/\gamma'$  Ni and Co-based superalloys should be carried out. During conditions of overheating regimes during a flight, partial dissolution of  $\gamma'$  can occur. These localized high-temperature regimes could affect the appliances' creep resistance and fatigue strength due to the partial dissolution and coarsening of  $\gamma'$  particles.

Solution treatment and cooling rates significantly affect the morphology, size, and content of the precipitated phases in these superalloys [4], thereby affecting the mechanical and hot-corrosion properties of the material. Lower cooling rates like (AC & FC) causes coarsening of the  $\gamma'$  precipitate, forming a multimodal distribution of precipitates throughout the microstructure. Therefore, the influence of the cooling rates after solution treatment on the microstructures, mechanical properties, and hot corrosion resistance of superalloys should be deeply researched. [4]

This work represents a detailed microstructural study of the effect of various cooling rates like WQ, AC, and FC on  $\gamma/\gamma'$  Co/Ni-based superalloy. Also, the effect of varying percentages of Cr on the microstructure, lattice misfit, and hardness values has been investigated. To investigate the morphological evolution in Co/Ni-based superalloys, they were divided into two groups,

I – studying the morphological changes with varying percentages of Cr as 0, 10, 20 at%.

II – studying the morphological changes in  $\gamma'$  by quenching the solutionized alloys in various cooling rates like WQ, AC, and FC.

Comparison with the commercially available age-hardenable Co/Ni-based superalloys is made by considering the factors like  $\gamma'$  size,  $\gamma'$  volume fraction, and  $\gamma'$  solvus temperature. Hardness values are also compared to get an idea of the strength of the alloys. The effect of the cooling rate is studied on alloys solutionized at 1150°C and 1200°C and cooled by WQ, AC, and FC. In contrast, the effect of alloying Cr is also studied on heat-treated alloys.

This study is expected to be instructive and helpful for designing and developing low-density W-free Co/Ni-based superalloys.

## CHAPTER 2

### LITERATURE REVIEW

#### **2.1 Novel Cobalt-based $\gamma/\gamma'$ Alloys**

Cobalt-based alloys possess higher oxidation, corrosion, and wear properties than Ni-based superalloys. It was reported that Co-W binary system forms a closed-packed  $\text{Co}_3\text{W}$  with  $\text{DO}_{19}$  structure, whereas the Co-Al binary forms a metastable  $\text{Co}_3\text{Al}$  with an  $\text{L}1_2$  ordered structure. Sato et al. have reported that a stable  $\text{Co}_3(\text{Al},\text{W})$   $\text{L}1_2$  ordered precipitate can form by adding W to the Co-Al binary system.[1] However, the ternary Co-Al-W system has a small  $\gamma + \gamma'$  phase field. Hence, Ni is added as the alloying element to increase the  $\gamma + \gamma'$  phase field in the ternary Co-Al-W system. For better creep properties at high temperatures, it is essential to have a higher  $\gamma'$  solvus temperature. Alloying additions like Ta, Ti, Al, Nb, V, etc., can increase the volume fraction and solvus temperature of  $\gamma'$  precipitates.

The recent discovery of  $\text{L}1_2$  precipitate  $\text{Co}_3(\text{Al}, \text{W})$  in 2006 by Sato et al. has gained tremendous interest in the field of superalloys due to their potential to overcome the drawbacks of Ni-based superalloys.

Table 2.1: Physical properties of Co and Ni based superalloys [2]

<b>Property</b>	<b>Typical ranges of Ni-based</b>	<b>Typical ranges of Co-based</b>
Density	7.6 – 9.1 g/cc	8.3 – 9.4 g/cc
Melting temperature	1310 – 1450 °C	1315 – 1495 °C
Elastic modulus	Room T: 210 GPa 800 °C: 160 GPa	Room T: 211 GPa 800 °C: 168 GPa
Thermal expansion	8 – 18 x 10 <sup>-6</sup> /°C	12.1 – 16 x 10 <sup>-6</sup> /°C
Thermal conductivity	Room T: 9 – 11 W/m-K 800 °C: 22 – 23 W/m-K	Room T: 10 – 13 W/mK 800 °C: 25 W/mK

Table 2.2: Role of alloying elements in superalloys.[2]

Element	Ni-based	Co-based
Cr	<ul style="list-style-type: none"> <li>• Improves resistance to hot corrosion and oxidation properties</li> <li>• Facilitates <math>M_{23}C_6</math> and <math>M_7C_3</math> carbide formation</li> <li>• Solid-solution hardening is moderate</li> <li>• Moderately increases the volume fraction of <math>\gamma'</math> phase</li> <li>• Assist in the development of TCP phase formation</li> </ul>	<ul style="list-style-type: none"> <li>• Forms <math>M_{23}C_6</math> and <math>M_7C_3</math> carbides</li> <li>• Improves hot corrosion and oxidation resistance</li> <li>• Promote close-packed (TCP) phases</li> </ul>
Al	<ul style="list-style-type: none"> <li>• Solid-solution hardening is moderate</li> <li>• Promotes precipitation of <math>\gamma'</math></li> <li>• Increases resistance to oxidation</li> </ul>	<ul style="list-style-type: none"> <li>• Improves oxidation resistance</li> <li>• Forms intermetallic <math>\beta</math>-(CoAl)</li> </ul>
Ti	<ul style="list-style-type: none"> <li>• Moderate solid-solution hardening</li> <li>• <math>\gamma'</math> precipitation</li> <li>• Promotes precipitation of TiC phase</li> </ul>	<ul style="list-style-type: none"> <li>• TiC carbide precipitation</li> <li>• Formation of <math>Co_3Ti</math> intermetallic</li> <li>• Formation of <math>Ni_3Ti</math> with sufficient Ni</li> <li>• Reduces surface stability</li> </ul>
Co	<ul style="list-style-type: none"> <li>• Raises <math>\gamma'</math> solvus temperature</li> <li>• Moderately increases the volume fraction of <math>\gamma'</math> phase (some alloys)</li> </ul>	Not applicable
Ni	Not applicable	<ul style="list-style-type: none"> <li>• FCC stabilizer</li> <li>• Decreases hot corrosion resistance</li> </ul>
W	<ul style="list-style-type: none"> <li>• High solid-solution hardening</li> </ul>	<ul style="list-style-type: none"> <li>• Solid-solution hardening</li> <li>• Formation of <math>Co_3W</math> intermetallic</li> </ul>

	<ul style="list-style-type: none"> <li>Moderately increases volume fraction of <math>\gamma'</math> phase</li> <li>Promotes formation of <math>M_6C</math> carbide</li> <li>Increases density</li> <li>Promote TCP phases (<math>\sigma, \mu</math>)</li> </ul>	<ul style="list-style-type: none"> <li>Promotes TCP phases</li> </ul>
Ta	<ul style="list-style-type: none"> <li>High solid-solution hardening</li> <li>Promotes the precipitation of TaC carbide.</li> <li>Largely increases the formation of <math>\gamma'</math> phase</li> </ul>	<ul style="list-style-type: none"> <li>MC and <math>M_6C</math> carbide precipitation</li> <li>Formation of <math>Co_2Ta</math> intermetallic</li> <li>Reduces surface stability</li> </ul>
Nb	<ul style="list-style-type: none"> <li>High solid-solution hardening</li> <li>Largely increases the volume fraction of <math>\gamma'</math> phase</li> <li><math>NbC</math> carbide formation</li> <li>Facilitates the formation of <math>\gamma'</math> phase</li> <li><math>\gamma''</math> precipitation</li> <li><math>\delta-Ni_3Nb</math> precipitation</li> </ul>	<ul style="list-style-type: none"> <li>MC and <math>M_6C</math> carbide precipitation</li> <li>Formation of <math>Co_2Nb</math> intermetallic</li> <li>Reduces surface stability</li> </ul>

## 2.2 Low Density, High-Temperature Co-based Superalloys

In the early development of  $\gamma/\gamma'$  Co-Al-W superalloys, the addition of W (19.3 g/cm<sup>3</sup>), up to 25 wt. percent, was critical. W was considered to be required for the  $\gamma/\gamma'$  microstructure to be stable. [3] A series of papers published in 2015 indicated that stabilisation of the  $\gamma/\gamma'$  microstructure in the Co-Al-Mo system may be achieved by adding a modest quantity of Nb or Ta, but not by adding W. [3] W-free Co base superalloys, also known as 'Low-Density Co-based superalloys,' were the name given to these alloys. The bulk densities of these alloys are 7.8–8.6 g/cm<sup>3</sup>. K. Chattopadhyay et al. were the first to discover them, and they were successful at achieving

high-temperature strength (at 870°C) > 0.6 GPa,  $\gamma'$  solvus temperature exceeding 1100 °C, and densities between 7.8 and 8.6 g/cm<sup>3</sup>.

Initially, these new generation alloys were stabilized by the addition of small amounts of Nb and Ta; some of them are described as follows:

### **2.2.1 Co-10Al-5Mo-2Nb at.%**

The alloy was prepared by melting, i.e., Vacuum Induction Melting in Al<sub>2</sub>O<sub>3</sub> crucible in Ar gas under operating pressure of 600Torr. Melting temperature: 1650°C to 1750°C. Aging treatment was done @ 800°C for 2h. Cuboidal  $\gamma'$  precipitates ~40nm size with  $\gamma'$  volume fraction of ~54% were formed after the aging treatment. The alloy has a mass density of 8.36g/cc, i.e., 1.2g/cm<sup>3</sup> lower than the Co-8.8Al-9W base alloy. The mean precipitate size is measured to be 40 ± 20 nm.[4]. Upon aging at 800°C beyond 35h, the  $\gamma/\gamma'$  microstructure decomposes to the following equilibrium phases:[4]

- FCC  $\gamma$ -Co
- B2 ordered CoAl,
- DO<sub>19</sub> ordered Co<sub>3</sub>(Nb, Mo)

The major drawback of these alloys is low  $\gamma'$  solvus temperature. The  $\gamma'$  solvus was measured to be ~866°C, lower by ~124°C than the Co-8.8Al-9W superalloy.

### **2.2.2 Co-10Al-5Mo-2Ta**

The  $\gamma'$  phase is further stabilized by the substitution of Ta for Nb. Cuboidal precipitates result during ageing at 800°C for 10 hours (58 percent volume fraction). In comparison to the Co-10Al-5Mo-2Nb alloy, the solvus temperature increased by 62°C to 928°C. The rise in Al partitioning to  $\gamma'$  phase is induced by the robust partitioning of Ta into  $\gamma'$ . The presence of needle-shaped Co<sub>3</sub>Mo intermetallic compound and  $\gamma'$  precipitates at 9% Mo results in the coexistence of needle-shaped Co<sub>3</sub>Mo intermetallic compound and  $\gamma'$  precipitates. Ta can strongly partition to and raise the temperature of the solvus. The Co-12.9Al-5.9Mo-3.7Ta measured composition

supports the  $\gamma'$  stoichiometry  $\text{Co}_3(\text{Al, Mo, Ta})$ . [5]

### 2.2.3 Co-30Ni-10Al-5Mo-2Ta-xTi ( $x = 0, 1, 2$ and $4$ at %)

After ageing at  $900^\circ\text{C}$ , Ta (2 at.%) increases the  $\gamma'$  solvus by  $110^\circ\text{C}$  and its volume fraction by 20% in Co-9Al-9W based superalloy. In addition to Ta, Ti has been proposed as an alloying additive in Co-Al-W alloys.  $\text{Co}_3\text{Ti}$  is a stable phase with an  $\text{L}1_2$  structure in the binary Co-Ti system. However, the low solvus temperature of  $\text{Co}_3\text{Ti}$  ( $815^\circ\text{C}$ ) and its tendency to precipitate with cellular shape prevent Co-Ti-based alloys from being employed as a high-temperature material. [6]

In the as-solutionized state, heat treatment of these alloys produces an average precipitate size ( $\langle r \rangle$ ) of 14nm. A plot of the size of the precipitate and its number density ( $N_v$ ) as a function of Ti content is shown in Figure 2.1 (a). Furthermore, the  $N_v$  drops with an increase in Ti content.

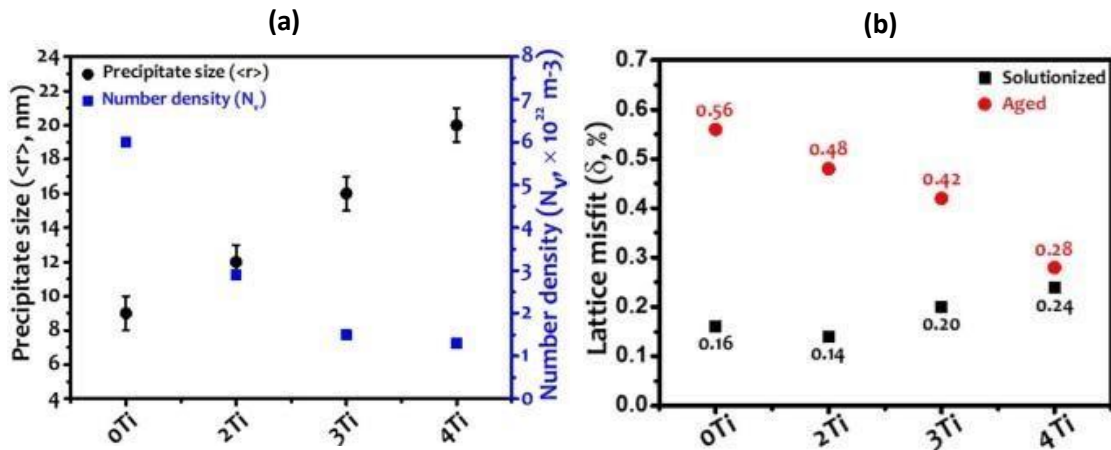


Fig. 2.1: (a) The average  $\gamma'$  precipitate size ( $\langle r \rangle$ ) and their number density ( $N_v$ ) as a function of Ti content in the alloy (b) Variation of  $\gamma / \gamma'$  lattice misfit with Ti content in the alloy for as-solutionized and after aging at  $900^\circ\text{C}$  for 50h.[6]

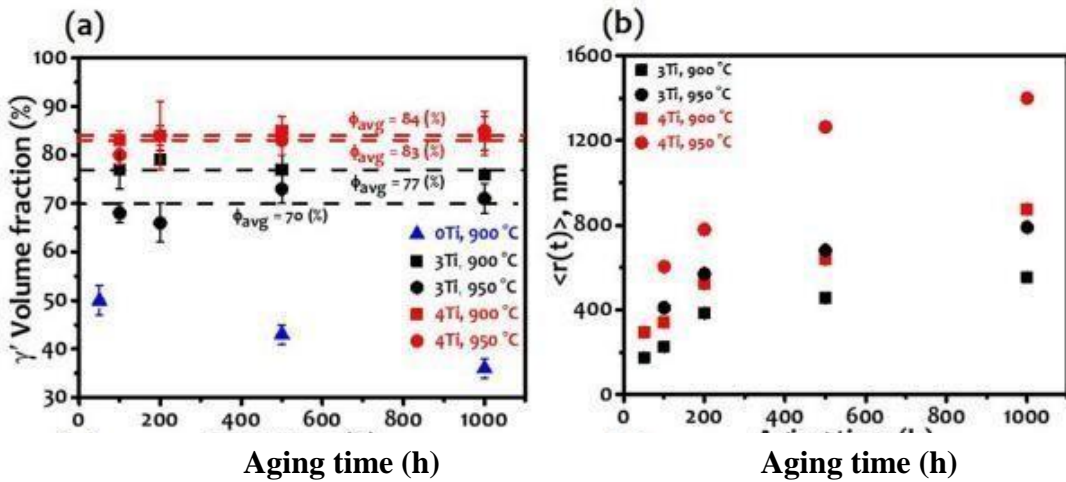


Fig. 2.2: Temporal evolution of (a)  $\gamma'$  volume fraction (%), (b) Average precipitate size ( $\langle r(t) \rangle$ ) in 3Ti and 4Ti alloys during isothermal aging at 900 °C and 950 °C. [6]

The  $\gamma'$  solvus temperature increases from 1014°C for 0Ti alloy to 1166°C for 4Ti alloy. When compared to Co-9.2Al-9W and Ni-based Waspaloy, it is 18% and 13% higher, respectively. After 1000 hours of ageing at 900°C, the observed  $\langle r(t) \rangle$  values for 3Ti and 4Ti were 555 nm and 875 nm, respectively. Similarly, after 1000 hours of age at 950°C, the  $r(t)$  of 3Ti and 4Ti alloys were observed to be 790 nm and 1400 nm, respectively. [6]

### 2.3 Coarsening of Precipitates

The resistance to coarsening of  $\gamma'$  precipitates determines the alloy's phase stability and mechanical characteristics. In Ni-based superalloys, the dissolving and coarsening kinetics of these precipitates, as well as their associated processes, have been thoroughly explored. Coarsening of these precipitates follows the classical Ostwald Ripening Mechanism based on Lifshitz-Slyozov and Wagner (LSW) theory.[7] According to this theory, governing principle for coarsening is due to the diffusion of solute elements in the matrix.

The LSW theory has assumptions such as [7]

- (i) Both the phases present in the system are dilute solutions, and the dilute solution model can explain their thermodynamics
- (ii) The volume fraction of the precipitate phase is close to zero so that there is no inter-precipitate interactions
- (iii) The system is at the equilibrium stage where there is no solute supersaturation

### **2.3.1 Factors affecting coarsening of precipitates**

Some factors significantly affect the coarsening kinetics of the precipitates and are explained below:

#### **a. Volume fraction of precipitates**

In many Ni or Co-based superalloys, the volume fraction of the precipitates is usually more than 60%. [7] A high volume fraction can lead to the alloy's high strength as the inter-particle distance is less and more stress is required for the dislocations to cut through these particles. However, in many solid solutions, a high-volume fraction of the precipitates can also lead to the joining of the precipitates, this phenomenon is called 'coalescence' [7], [14]. The driving force for the coalescence comes from the removal of the highly strained region of the  $\gamma$  matrix between the two  $\gamma'$  precipitates. The strain is due to the high lattice misfit at the  $\gamma/\gamma'$  interface. Coalescence is also affected by the annealing time and temperature. High annealing temperature and prolonged periods can cause the formation of irregular coarse  $\gamma'$  precipitates. [7]

#### **b. $\gamma'$ precipitate shape**

Competition between interfacial and elastic energy contributions could explain the evolution of free growth. [8] Because interfacial energy is proportional to surface area ( $r^2$ ), isotropic precipitate morphologies such as spherical shapes are encouraged. In contrast, The elastic energy of the precipitate is related to the volume of the precipitate, promoting elastic non-isotropic precipitate forms like cuboids, rods, or irregular shapes. [8] This energy interaction between the precipitate and the matrix leads to small, spherical-shaped precipitates where the interfacial energy is dominant, whereas, with the dominance of elastic energy, the shape transforms to cuboidal or plate-like having dendritic morphology. Lattice mismatch also majorly contributes to the precipitate shape. Lower lattice misfit offers high coherency at the  $\gamma/\gamma'$  interface leading to the formation of a spherical shape. As the precipitates grow, cube, octocube, or plate-like shapes are favored indicating a higher lattice misfit and increase in the elastic energy

contribution. Therefore, the morphology change is described as a transformation of 'sphere → cube → octocube → octodendrite → dendrite'. [8]

#### 2.4 $\gamma'$ dissolution and formation of cooling precipitates

$\gamma'$  dissolution behavior is studied extensively on Ni-based superalloys to optimize the solution heat treatment. Tianyou Wang et al. [8], in their dissolution studies on IN100 and DS Rene 125 Ni-based superalloys, reported the formation of dual-phase  $\gamma'$  morphology. It forms with an increase in solutionizing time and temperature where the primary  $\gamma'$  coarsens and partially dissolves from a cubic morphology to spherical or quasi-spherical morphology. [8] This is justified in Figure 2.3, which reveals the partial dissolution process of primary  $\gamma'$  by splitting coarse  $\gamma'$  into smaller fragments controlled by the interfacial energy along with the formation of secondary  $\gamma'$  cooling precipitates at high solutionizing temperatures. Higher solutionizing temperatures in the  $\gamma'$  super-solvus regime can offer a high driving force for the formation of cooling precipitates.

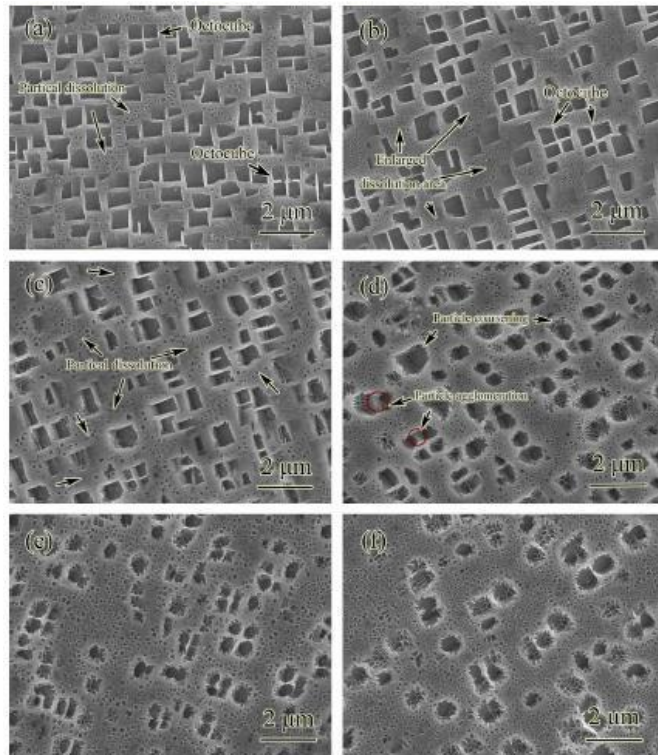


Fig. 2.3: Microstructures of  $\gamma'$  precipitates heated at (a) 1160°C for 15 min; (b) 1160°C for 30 min; (c) 1180°C for 30 min; (d) 1180°C for 45 min; (e) 1200°C for 15 min; (f) 1200°C for 45 min. [8]

N. El-Bagoury et al. [9] have reported the  $\gamma'$  precipitate evolution of IN100 superalloy at different heat treatment conditions. Solution heat treatments are done at 1120°C, 1180°C, and

$1220^{\circ}\text{C}$  for 1.5h revealing the  $\gamma'$  morphology to change from a fine cuboidal shape to coarse spherical ones with the increase in solutionizing temperature (Fig. 2.4). The cooling medium also affects the volume fraction of the precipitates. Figure 2.4 shows an increase in the volume fraction of the precipitates for WQ samples than for AAC samples. At low cooling rates, high solute diffusion in the matrix produces coarsening of primary  $\gamma'$  and a decrease in its volume percentage. With high solutionizing temperature and high cooling rates, however, the secondary  $\gamma'$  volume portion increases.

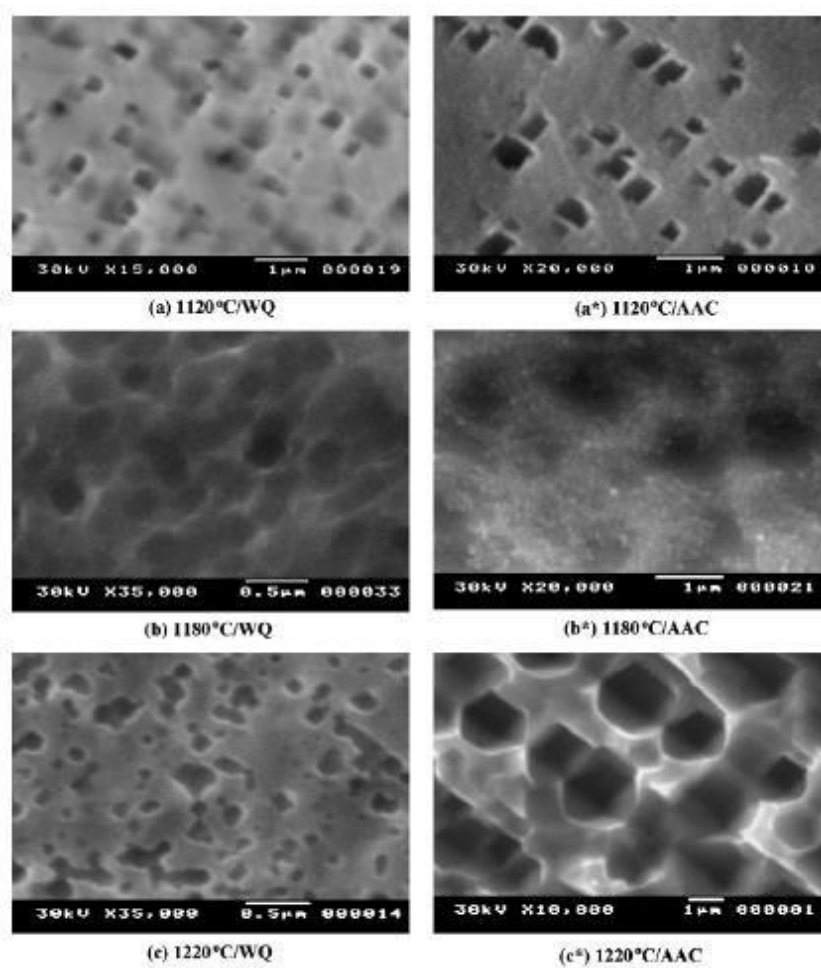


Fig. 2.4: Effect of solution treatment conditions on  $\gamma'$  precipitates. [9]

The lattice mismatch between the  $\gamma$  and  $\gamma'$  phases is directly affected by the lattice parameter 'a' of individual phases. It is indirectly affected by elemental segregation and heat treatment conditions. Mohammad Mehdi Barjesteh et al. [10], in their work, have reported an increase in the lattice mismatch with an increase in holding time, while the lattice mismatch decreases with an increase in the annealing temperature.

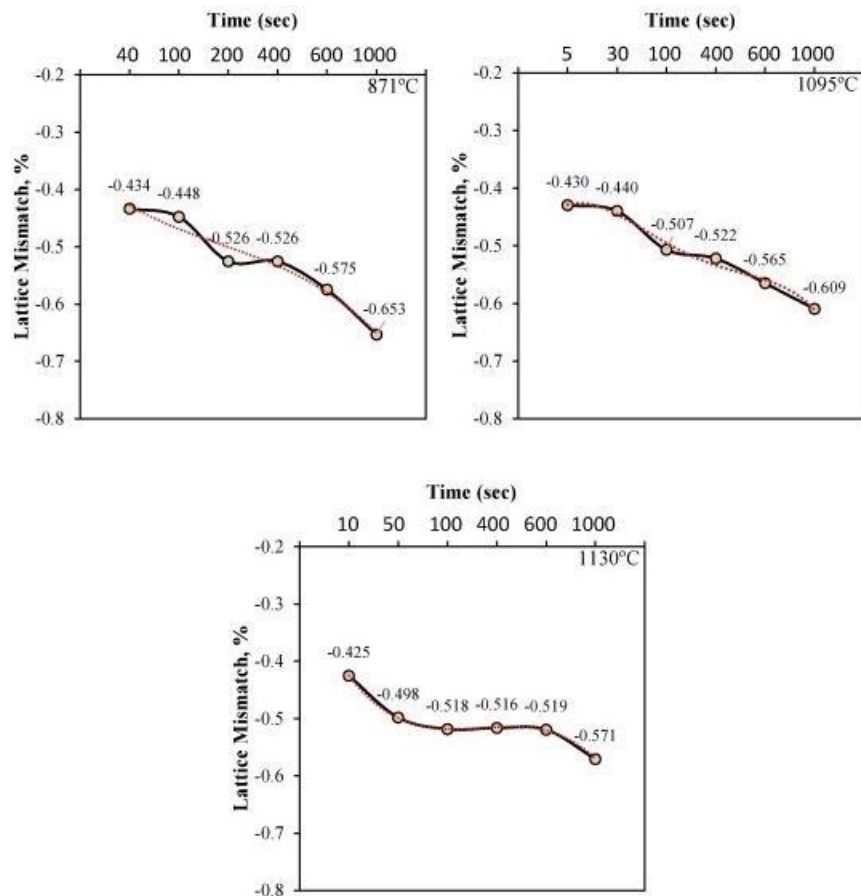


Fig. 2.5: Variations of  $\gamma$ - $\gamma'$  lattice mismatch with heat treatment temperature and time for Rene<sup>®</sup>80. [10]

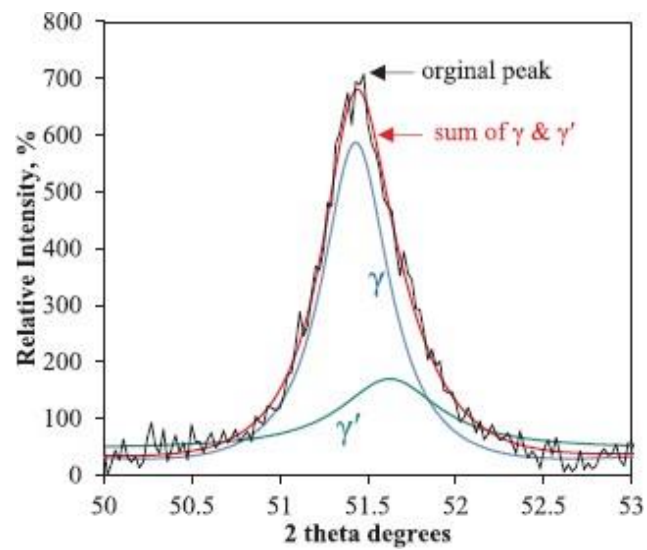


Fig. 2.6: Deconvolution of the corresponding peaks to the  $\gamma$  and  $\gamma'$  phases. [10]

Deconvolution of the peak was done as the peaks corresponding to  $\gamma$  and  $\gamma'$  phases overlap. [10] This deconvolution was done based on equation 1.

$$y = yo + A[m_u \frac{2 \times w_L}{\pi \times (x - x_C)^2 + w_G^2} + (1 - m_u) \frac{\sqrt{4 \ln 2}}{w_G \sqrt{\pi}} e^{-\frac{4 \ln 2(x - x_C)^2}{w_G^2}}] \dots\dots (3)$$

where,

peak position – x

peak height – h

shape factor -  $m_u$

Gaussian FWHM –  $w_G$

Lorentzian FWHM -  $w_L$

The deconvolution of the peaks can be done and analyzed in Origin Pro software.

## 2.5 Effect of cooling rates on $\gamma'$ precipitation behavior

H. R. Abedi et al. [11], in their work on the study of precipitation behavior in different cooling rates, have reported a shift of the DSC curve to the left, as shown in Figure 2.7, thus indicating an increase in the precipitation rate with increase in cooling rates.

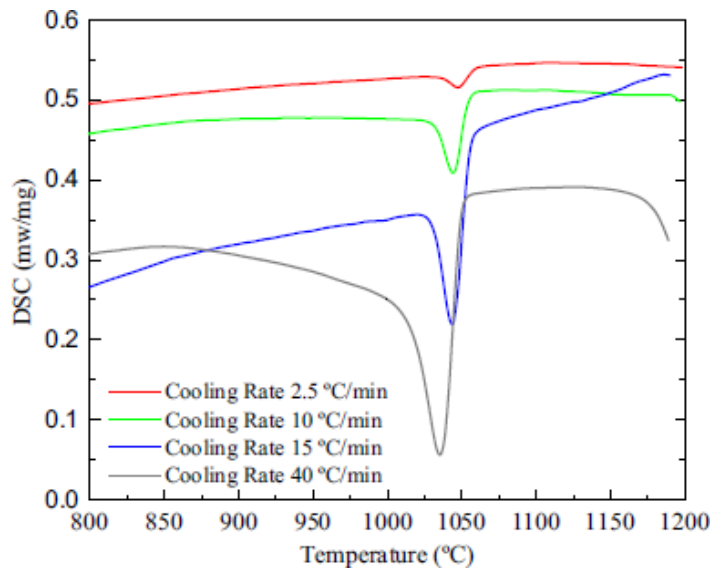


Fig. 2.7: DSC curves demonstrating  $\gamma'$  precipitation peaks during cooling. [11]

Temperature and time-dependent enthalpy were used to study the precipitation behavior by plotting various graphs of fraction of precipitation (F) vs. temperature (T) and the precipitation rate ( $dF/dt$ ) vs. temperature (T).

The fraction of the phase transformation  $F(T)$  that occurred at a given temperature was determined as [11]

$$F(T) = \frac{A(T)}{A(T_f)} \dots \quad (4)$$

where,

$A(T)$  – area of the peak between the onset temperature  $T_i$  (beginning of precipitation) and temperature  $T$  (any temperature on the signal)

$A(T_f)$  – area under the peak between  $T_i$  and the end temperature  $T_f$  (end of precipitation)

The precipitation rate ( $dF/dt$ ), which is correlated to the cooling rate  $\beta$  is given by [11]

H. R. Abedi et al. [11] reported the activation energy contribution to the precipitation and have calculated the activation for their developed alloy CoWAlloy1 to be 1775 kJ/mol. The calculation is done based on the equation [11]

$$Q = -\frac{\ln \left( \frac{T_F^2}{\beta} \right)}{\left( \frac{1}{RT_F} \right)} \dots \dots \dots \quad (6)$$

where,

$T_F$  – the temperature at which the maximum precipitation rate ( $dF/dt$ ) occurs

R – universal gas constant in J/Kmol

The activation energy determined by H. R. Abedi et al. [11] for this alloy is much higher than those for the Ni-based superalloys, indicating a lower atomic diffusion rate in Co-based superalloys as compared to Ni-based superalloys.

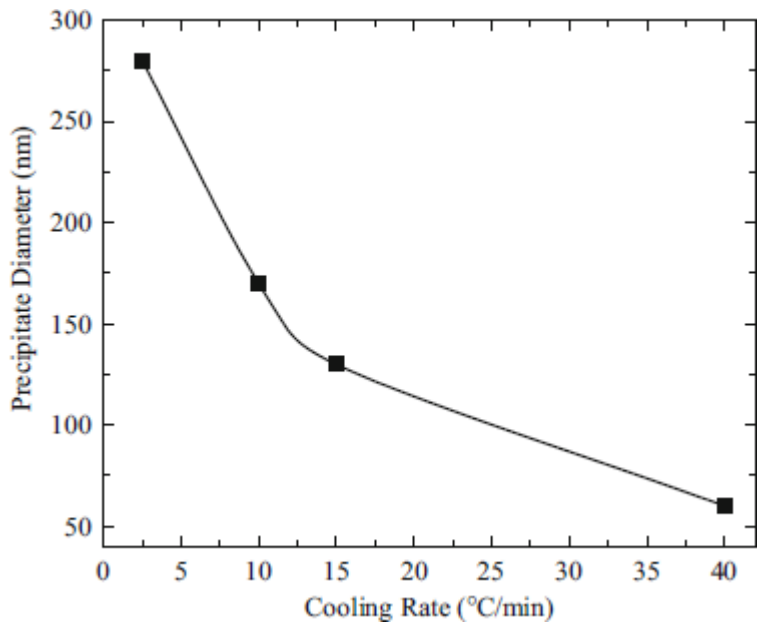


Fig. 2.8: Average diameter of  $\gamma'$  precipitates as a function of cooling rate. [11]

Figure 2.8 confirms that increasing the cooling rate decreases the  $\gamma'$  precipitate size. H. R. Abedi et al. [11] have found that increasing the cooling rate from  $2.5^{\circ}\text{C}/\text{min}$  to  $400^{\circ}\text{C}/\text{min}$  decreased the particle size from  $280\text{nm}$  to  $60\text{nm}$ .

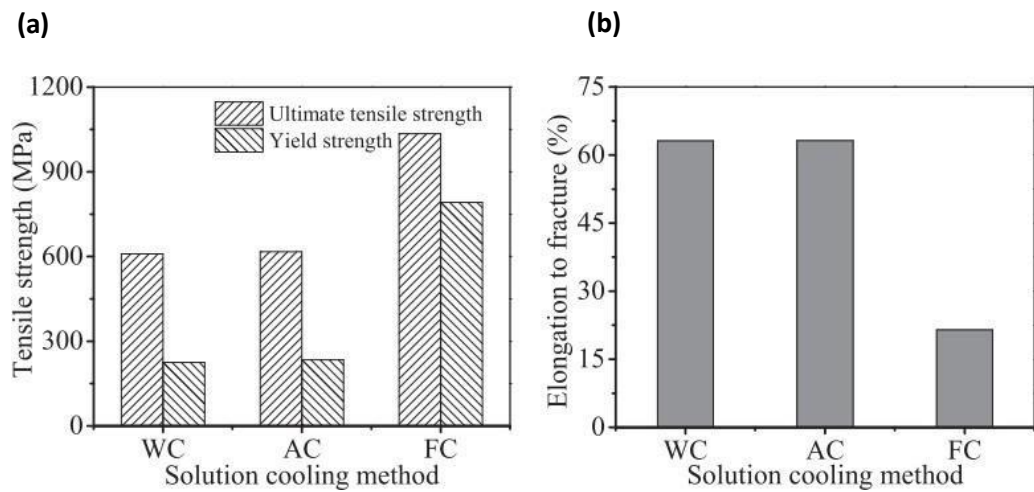


Fig. 2.9: Influence of cooling methods on the (a) tensile, (b) elongation and (c) microhardness values of GH4169 Ni-based superalloy.[12]

Figure 2.10 describes the work of Dao-Guang et al. [12] that the strength and hardness of the material increase with decreasing solutionizing cooling rate and is maximum for FC samples. This is because of the formation of secondary  $\gamma'$  precipitates during FC, which is responsible for the higher strength of the alloy. [12]

High cooling rates undergo precipitate shearing rather than Orowan looping, which is a high cooling rate mechanism.

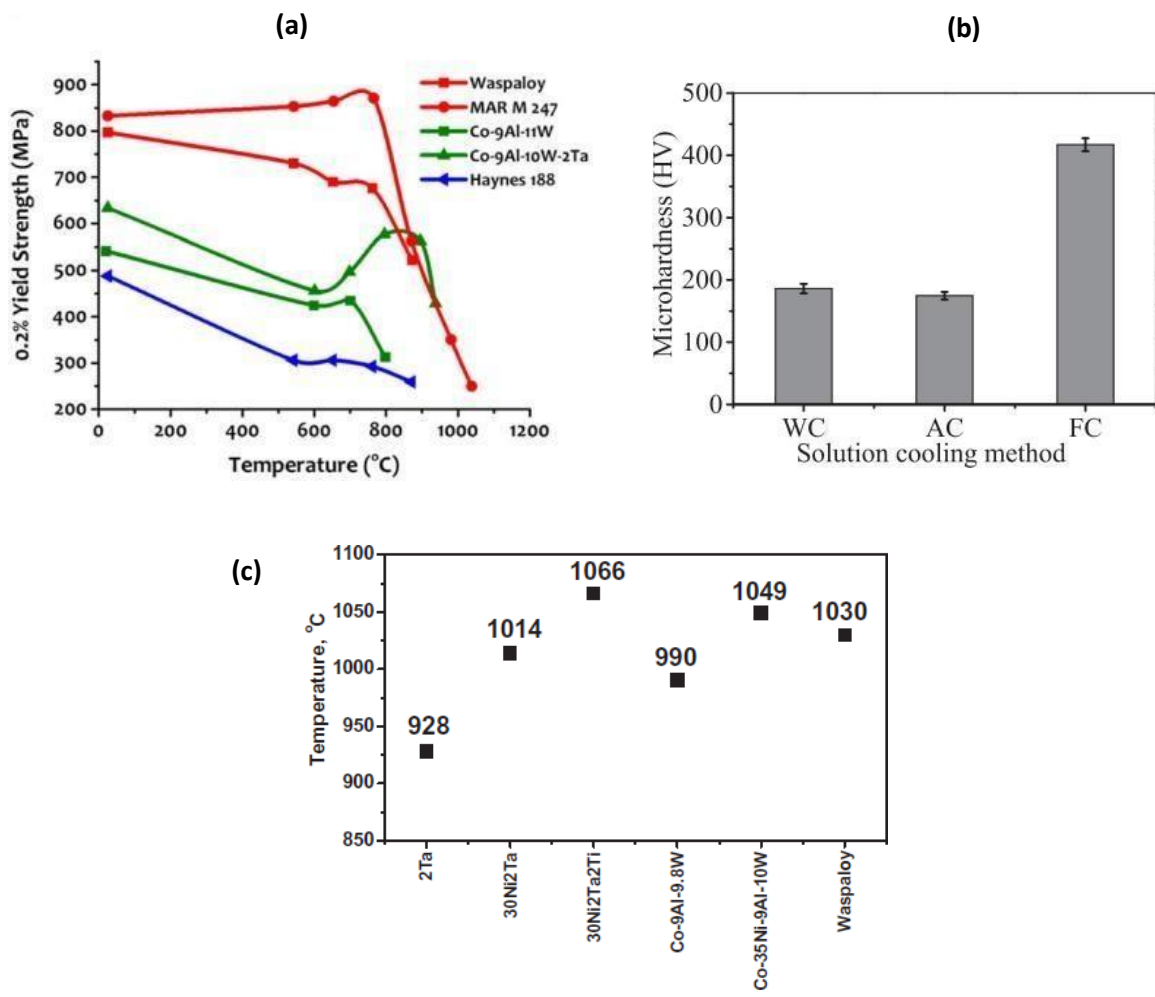


Fig. 2.10: (a) 0.2% proof stress of Waspaloy, MAR M 247, Co-9Al-11W, Co-9Al-10W-2Ta and Haynes 188 superalloys with temperature and (b) solvus temperature of Co-10Al-5Mo-2Ta, Co-30Ni-10Al-5Mo-2Ta, Co-30Ni-10Al-5Mo-2Ta-2Ti, Co-9Al-9.8W alloy, Co-35Ni-9Al-10W alloy and nickel-based superalloy (Waspaloy).[13]

Figure 2.10 shows the commercially used Ni-based superalloy (Waspaloy) has a high yield strength anomaly at a higher temperature where the YS increases initially then decreases with an increase in temperature, reaching a peak at 700 MPa at  $T < 800^{\circ}\text{C}$ . On the contrary, for Co-based superalloys, the peak reaches YS  $\sim 900$  MPa at  $800^{\circ}\text{C}$ . This shows that a Co-based superalloy can attain higher strength values even at higher temperatures. [13]

## 2.6 Effect of lattice misfit on precipitate size and morphology

The lattice misfit is an important issue since it is linked to the morphology of the  $\gamma'$  phase. By changing the lattice misfit to 0-0.2%, 0.5-1%, and >1.25%, the shapes of the  $\gamma'$  phase shift from spherical, cuboid, and plate-like, respectively. [14] The influence of Cr and Al:Ti on several newly discovered Ni and Co-based superalloys was investigated by K.A. Christofidou et al. [14] According to their findings, the alloy system's hardness value correlates with the lattice misfit between the  $\gamma$  and  $\gamma'$  phases, as illustrated in Figure 2.11.

The lattice misfit  $\delta$  (in %) is calculated as,

$$\delta = 2 \times \left[ \frac{a_{\gamma F} - a_\gamma}{a_{\gamma F} + a_\gamma} \right] \dots \quad (7)$$

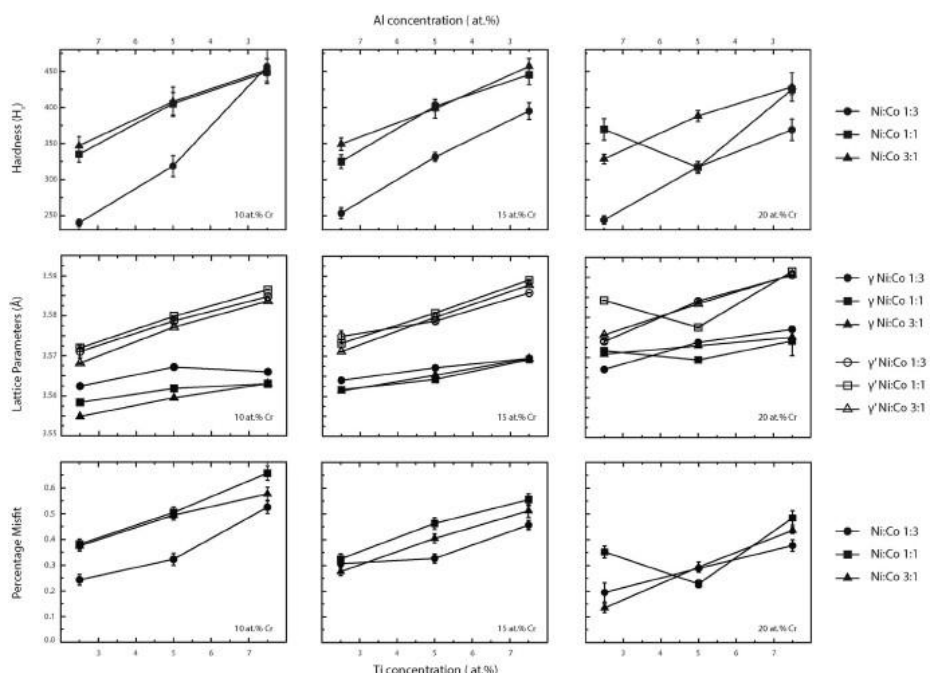


Fig. 2.11: Collective results showing the variation of the Vickers hardness, lattice parameters of the  $\gamma$  and  $\gamma'$  phases and lattice misfit as a function of the concentration of Ti (in at.%) in the alloys. [14]

As seen in Figure 2.11, there is a prominent variation in the misfit values by varying the alloying elements. The lattice misfit of the alloys drastically increases from ~0.2% to ~0.5% with an increase in the Ti content. In contrast, there is a drop in the lattice misfit with an increase in the %Cr content.[14] This is because Cr has a strong tendency to partition towards the  $\gamma$  phase, thereby increasing the lattice parameter of the  $\gamma$  phase ' $a_{\gamma}$ ' and reducing the lattice misfit value. In contrast, the lattice parameter of the  $\gamma'$  phase ' $a_{\gamma'}$ ' increases with an increase in the %Ti content, increasing the lattice misfit value as Ti partitions towards the  $\gamma'$  phase.[14]

However, from the hardness curve shown in Figure 2.5, for Al:Ti as 3:1, the hardness drops to a minimum of 250HV. The hardness is thus observed to be increasing with increasing Ti and Cr concentrations.[14]

Table 2.3: The lattice misfit, hardness and  $\gamma'$ -precipitate sizes of (i) Co-27.2Ni-3.1Al-8.1Ti-10.9Cr, (ii) Co-18.3Ni-3Al-7.8Ti-16.2Cr (iii) Co-17.3Ni-3.1Al-7.9Ti-21.5Cr. [14]

Sr. No	Alloy	Lattice misfit (%)	Hardness (HV)	$\gamma'$ precipitate size (nm)
i	10at% Cr	0.53	457	46.6
ii	15at% Cr	0.46	395	58.8
iii	20at% Cr	0.38	369	45.7

Table 2.3 reveal the relation between lattice misfit, hardness, and precipitate size of the alloy with increasing %Cr. It is observed that the hardness value decreases with a decrease in the lattice misfit and an increase in %Cr. The solutionization study conducted by K.A. Christofidou et al. for the above-mentioned nickel and cobalt-based superalloys as in Table 2.3 proves that there is a precipitation of  $\gamma'$  during cooling from 1200°C to RT by air cooling, having no change in the shape and morphology but a considerable change in the lattice misfit and hardness.

Also, as it is well known that the XRD peaks of  $\gamma$  and  $\gamma'$  overlap, it is necessary to separate the peaks to identify the individual phases and calculate the lattice parameters of these phases. Qizhi Gao et al. [15], in their work, have reported the separation of the peaks using deconvolution theory, where the high intensity (111) peak is fitted using the Voigt distribution function.

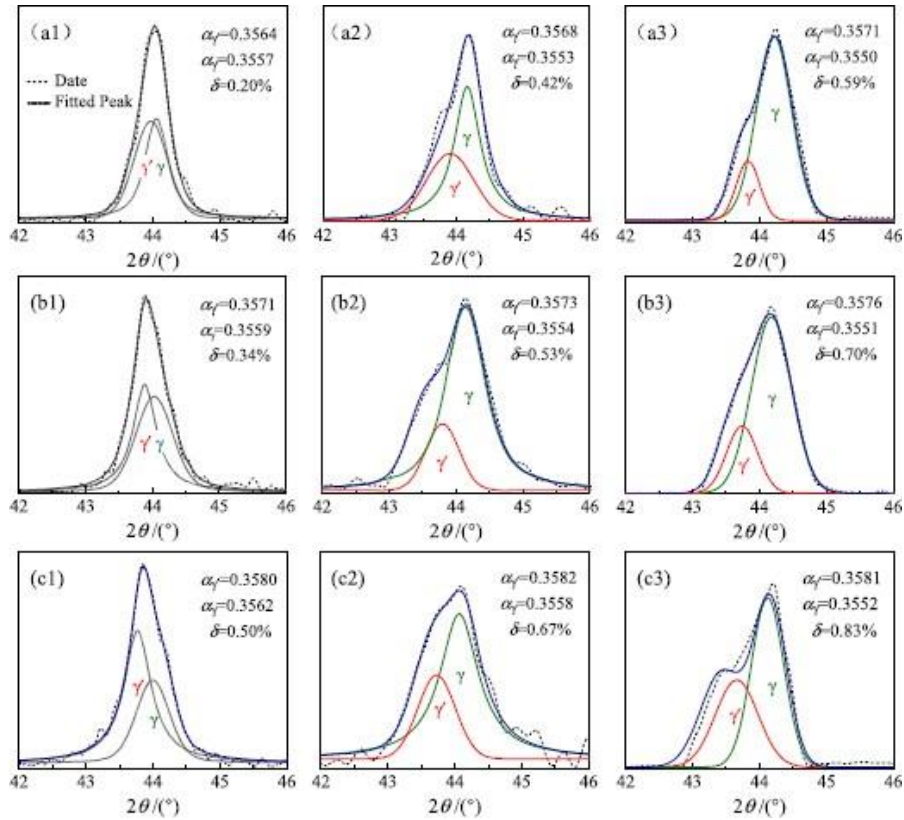


Fig. 2.12: XRD of (111) diffraction peaks of aged superalloys. [15]

It is evident from Fig. 2.12 that  $\gamma'$  occupies the lower theta position as it has a higher lattice parameter than the  $\gamma$  phase. The overlapped peaks are deconvoluted, showing a lattice misfit in the range 0.2~0.8%, which increases with increasing %Ti. [15]

The sign of the lattice misfit is also a deciding factor in the high-temperature strength properties of the materials. [16] Most Ni-based superalloys possess negative lattice misfits at room temperature with a magnitude of  $\sim 10^{-3}$ , whereas the misfit decreases further with an increase in temperature. However, Co-based superalloys exhibit high-temperature properties comparable to Ni-based superalloys. This is because of exhibiting a positive misfit at room temperature which further decreases with an increase in temperature but remains positive up to a temperature close to 1000 °C. [16] Some authors consider positive lattice misfit is favorable for dislocations to pile up and increase at the  $\gamma/\gamma'$  phase boundary and resist the  $\gamma'$  shearing. [17]

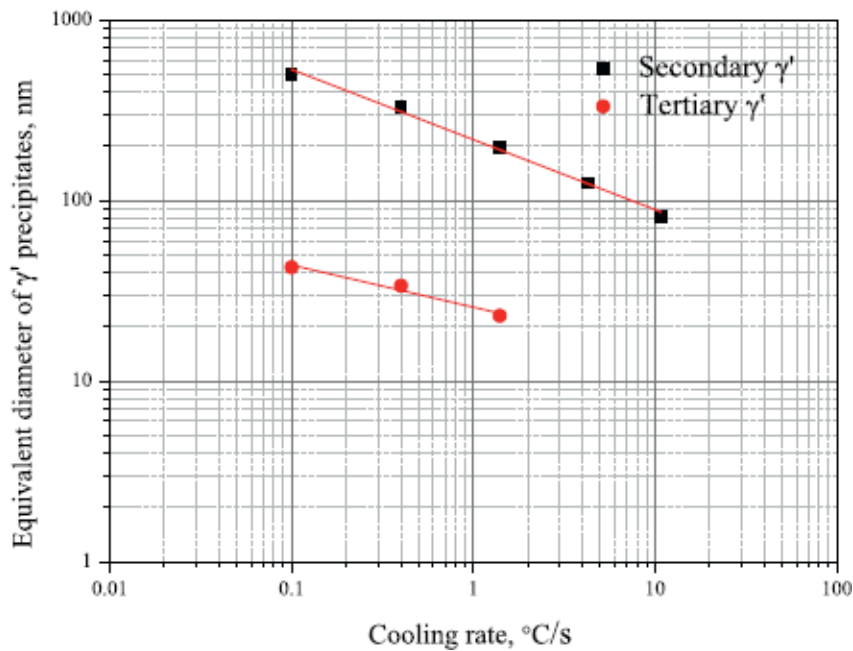


Fig 2.13: The mean size of secondary and tertiary  $\gamma'$  particles as a function of cooling rates showing an approximately linear relationship in the log-log plot. [18]

Guochao Huang et al. [18], in their study on the effect of cooling rates over nickel superalloys, have reported a decreasing trend in the size of secondary and tertiary  $\gamma'$  with an increase in the cooling rate. High cooling rates result in higher undercooling and smaller  $\gamma'$  size because of the increase in nucleation density due to higher supersaturation of the alloying elements. Lower cooling rates of  $0.1^{\circ}\text{C/s}$  exhibit a bimodal distribution of the precipitates, while higher cooling rates greater than  $0.1^{\circ}\text{C/s}$  exhibit a unimodal size distribution. [18]

The empirical formulas calculated by the linear regression of  $\gamma'$  size and corresponding cooling rates as given below help predict the size of secondary and tertiary  $\gamma'$  particles. [18]

For secondary  $\gamma'$  phase: [18]

$$\log(D_{\gamma'}) = 2.353 - 0.401 \times \log\left(\frac{dT}{dt}\right) \dots\dots\dots (8)$$

For tertiary  $\gamma'$  phase: [18]

$$\log(D_{\gamma'}) = 1.409 - 0.233 \times \log\left(\frac{dT}{dt}\right) \dots\dots\dots (9)$$

where,

$D_{\gamma'}$  - mean  $\gamma'$  size in nm.

$(\frac{dT}{dt})$  – cooling rate in  $^{\circ}\text{C}/\text{s}$ .

The slope of secondary and tertiary  $\gamma'$  precipitates is shown in Figure 2.7, with the tertiary  $\gamma'$  having a lower slope than the secondary  $\gamma'$ . This demonstrates that the tertiary is temperature-dependent as well as cooling rate-dependent.

## 2.7 Aging studies of Co-Ni-Al-Ti based superalloy

Qizhi Gao et al. have studied the microstructural evolution and the mechanical properties of Co-Ni-Al-Ti based superalloy. Five alloy compositions were studied with varying Al:Ti as 2:1, 3:1, and 5:1 with three quaternary alloys and two quinary alloys with alloying elements of 2at.% Cr and 2at.% Mo.[15]

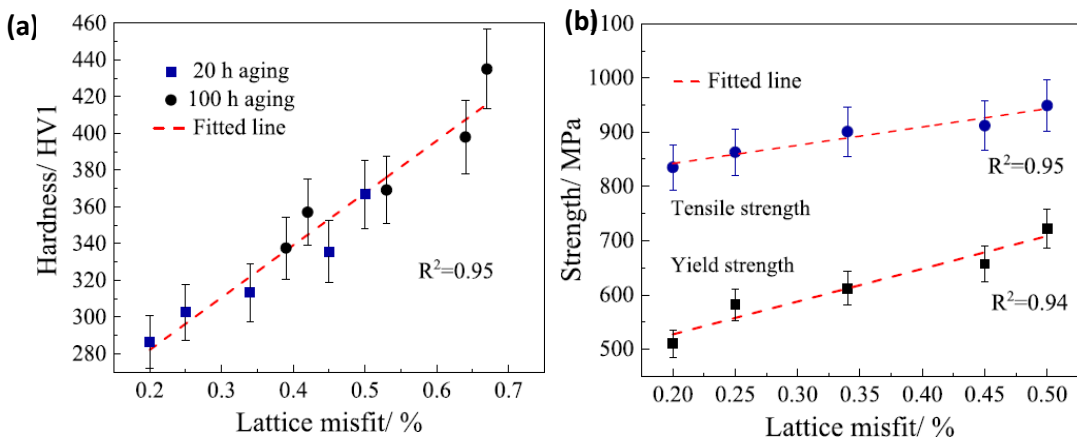


Fig. 2.14: Variation of (a) Vickers Hardness and (b) tensile and yield strength as a function of lattice misfit. [15]

The increasing trend of hardness and strength with lattice misfit is also observed with aging. The effect of cooling rate and the increase in %Cr on the microstructure, including size, shape and volume fraction of  $\gamma'$  phase and mechanical properties, was not explored.

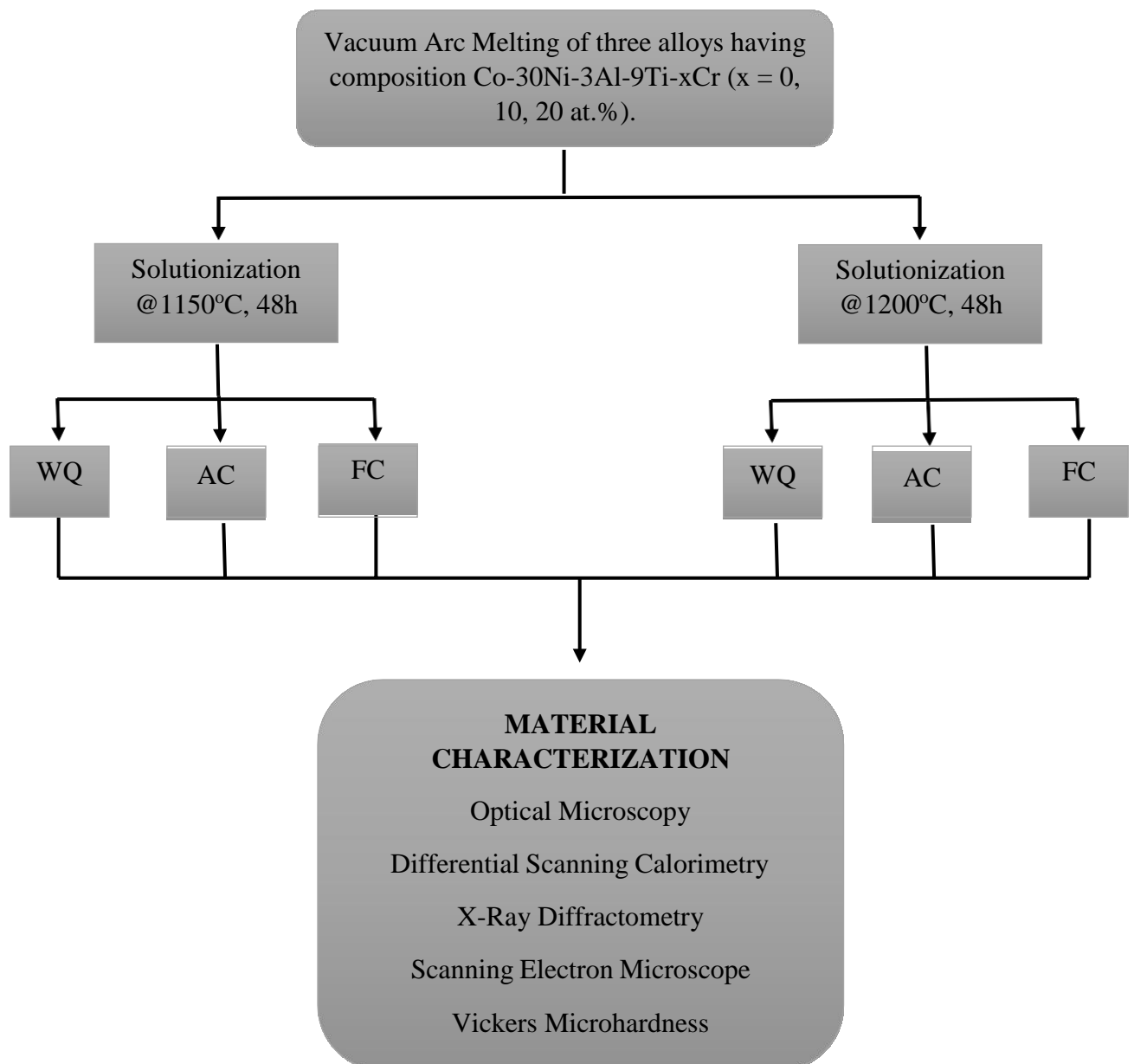
Table 2.4: Showing the comparison of various Co-based and Ni-based superalloys based on  $\gamma'$  solvus temperatures and hardness values after aging treatment.

<b>Alloy</b>	<b><math>\gamma'</math> solvus temperature (°C)</b>	<b>Hardness values (HV) (As-aged condition)</b>	<b>Reference</b>
Co-9Al-9W	990	~400	[1]
Co-30Ni-10Al-5Mo-2Ta-2Ti	1166	350 – WQ 450 - FC	[6]
Co-30Ni-10Al-5Mo-2Ta	1014	320 – WQ 440 - FC	[5]
Co-10Al-5Mo-2Ta	928	280	[5]
Co-30Ni-6.7Al-3.3Ti	760	440	[15]
Co-30Ni-7.5Al-2.5Ti-2Cr	700	330	[15]
Waspaloy	1030	350	[5]

## 2.8 OBJECTIVES

1. To understand the effect of the cooling rate on the microstructure of Co-30Ni-3Al-9Ti alloy solutionized at 1150°C & 1200°C and cooled by WQ, AC, and FC.
2. To study the effect of Cr on the precipitate evolution and lattice mismatch of the heat-treated alloys by varying Cr as 0at.% Cr, 10at.% Cr and 20at.% Cr.
3. To understand the change in mechanical properties with change in the microstructure by changing the cooling rate and increasing %Cr content.

## 2.9 PROCESS FLOW



## CHAPTER 3

### EXPERIMENTAL PROCEDURE

To achieve the objective of this work, four compositions of cobalt-based alloy with varying percentages of Cr and Al:Ti ratios were arc melted in a Vacuum Arc Remelting (VAR) furnace. The fabricated cobalt-based superalloys were then studied to understand the effect of heat treatment which is reviewed in detail by providing various microscopic and mechanical results to validate the study. Thus, this chapter introduces the materials and processing used and provides a theoretical overview of the characterization tools used in this thesis work.

#### **3.1 Materials**

The compositions of the quinary cobalt-based superalloys were selected to be of the form Co-Ni-Al-Ti-xCr ( $x = 0, 10, 20$  at.%) where three alloy compositions have varying at.% Cr with Al:Ti as 1:3. Another alloy with 20at% Cr and Al:Ti as 3:1 was also selected.

Table 3.1: Weight measurements of alloys used for the study in at% and wt%.

Element	A1-0at%Cr		A2-10at%Cr		A3-20at%Cr	
	at%	wt%	at%	wt%	at%	wt%
Co	60.2	62.38	50.2	52.48	50	53.06
Ni	27.7	28.58	28	29.18	18	19.02
Al	3.1	1.47	3.1	1.48	3	1.45
Ti	9	7.57	9	7.64	9	7.75
Cr	0	0	10	9.22	20	18.72
<b>Total</b>	<b>100</b>		<b>100</b>		<b>100</b>	

## 3.2 Alloy Preparation

### 3.2.1 Arc melting processing route

The elements, according to their corresponding wt.% as shown in Table 3.1, were processed by arc-melting casting technology using a VEC Vacuum Arc Remelting (VAR) furnace, as shown in Figure 3.1. This equipment uses a tungsten electrode and melts the elements at over 3000 °C. The melting occurs in a stainless-steel vacuum-enclosed chamber at a pressure of ( $\sim 10^{-3}$  Pa) to ( $\sim 10^{-5}$  Pa) in a copper crucible. The lower plate of the melting chamber is a water-cooled copper base plate. The as-cast specimens were identified as A1, A2, and A3 as per increasing at.% Cr as 0at.% Cr, 10at.% Cr and 20at.% Cr respectively.



Fig. 3.1: Vacuum Arc Melting Furnace (VEC Solutions)

## 3.3 Heat treatment design

The heat treatment was designed for the present work by considering the super-solvus temperatures for studying the dissolution of the  $\gamma'$  precipitates after solution heat treatment. For this purpose, Differential Scanning Calorimetric analysis (DSC) was performed in a 'Netzsch STA 449 F3 Jupiter' DSC instrument, as shown in Figure 3.2, to determine the phase transformation temperatures, i.e.,  $\gamma'$  solvus temperature during heating at a step heating rate of 10°C/min. The as-cast samples were solutionized in 1400°C box furnaces (VBCC-VEC and Indfurr furnace) as shown in Figure 3.3 at 1150°C and 1200°C (super-solvus temperatures) for 48h, followed by cooling under various mediums like water quenching, air cooling, and furnace cooling. The heating cycle of the solutionization heat-treatment is shown in Figure 3.4.



Fig. 3.2: Netzsch STA 449 F3 Jupiter make Differential Scanning Calorimetry (DSC)

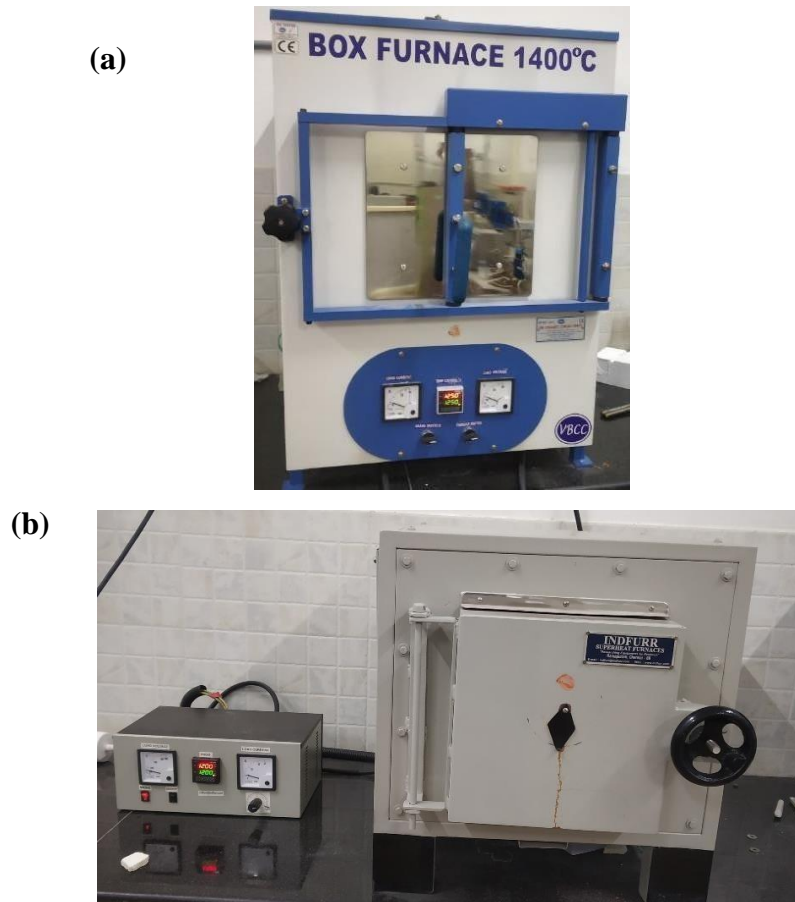


Fig. 3.3: Homogenization heat treatment of 4 alloy systems done in (a) VBCC Box furnace at 1200°C and (b) Indfurr Muffle Furnace at 1150°C

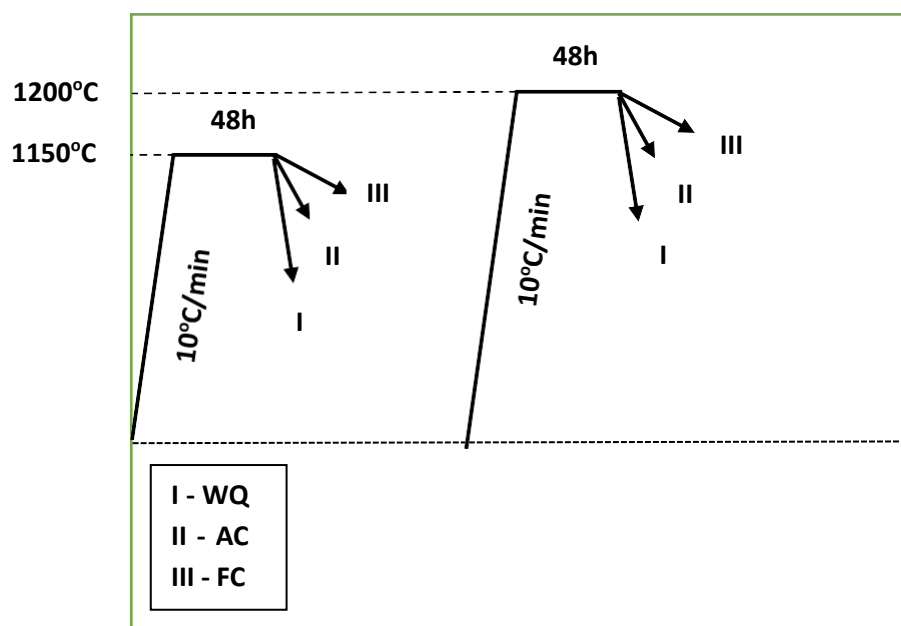


Fig. 3.4: Heat-treatment cycle.

All the four alloy specimens were homogenized in an Ar-gas-filled evacuated quartz capsule to prevent the specimens from reacting with the atmosphere and undergoing oxidation at high temperatures shown in Figure 3.5.



Fig. 3.5: Showing samples enclosed in vacuum sealed quartz tubes.

### 3.4 Microstructural Characterization

#### 3.4.1 High Flux X-Ray Diffractometer (HF-XRD)

#### High Flux Rotating Anode XRD

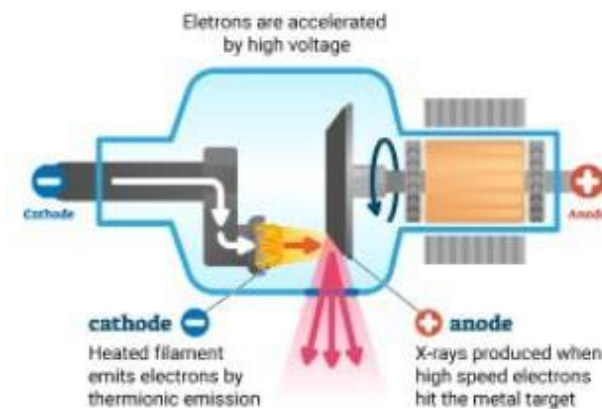


Fig. 3.6: Showing the schematic of the rotating anode of HF-XRD generator.  
[Google Image]

A High-Flux diffractometer is a specially designed tool to see the most delicate details in the specimen in the fastest timeframes. The high flux used in this diffractometer makes it unique and different from the conventional XRD, offering the best chance of detecting trace phases in the samples, thereby resolving weak diffracting crystals that would have been difficult to trace in a conventional XRD.

These rotating anode x-ray generators provide higher power than the conventional sealed tube x-ray generators, which provide a high number of photons required to analyze and characterize the most challenging samples.

The HF-XRD system generates a small and very dense X-ray beam targeting the critical area of interest and can detect tiny crystals less than  $10\mu\text{m}$  in size.



Fig. 3.7: Rigaku SmartLab HF-XRD generator.

#### **Benefits of High Flux XRD for diffraction studies:**

- Faster, accurate, high-quality data collection
- Higher throughput
- Improved ability to investigate small samples
- Enhanced ability to resolve large unit cells, twins, or incommensurate lattices
- More easily detects trace phases
- Maximize synchrotron time
- Proven reliable technology

XRD characterization of the samples was done using the HF-XRD generator, as shown in Figure 3.7. The high flux x-ray source of Cu-K $\alpha$  (=1.540598 Å) was taken to characterize the samples for the diffraction angles 20° – 120° providing a mean scan step size of 0.02° and a scan speed of 1°/min. The as-generated XRD plots were analyzed using PANalytical X'pert High Score Plus software. The software was used to identify the phases and crystal structure of the samples. Lattice parameters for each as-cast and heat-treated sample were calculated from the peaks measured by the XRD plots. The lattice parameter (a) is calculated by the Braggs's law given as,

where,

n – constant (taken as 1)

$\lambda$  – wavelength of x-ray source (Cu-K $\alpha$  = 1.540598 Å)

d – inter-planar spacing

$\theta$  – diffraction angle in degrees

$h, k, l$  – lattice indices

The lattice mismatch between  $\gamma/\gamma'$  interface is thus calculated by the lattice parameter of individual phases given by the following formula,

$$\delta = 2 \times \frac{a_{\gamma F} - a_\gamma}{a_{\gamma F} + a_\gamma} \dots \quad (12)$$

An alternative formula for calculating the lattice mismatch by the difference in d-spacing of the individual peak can also be done using the formula,

$$\delta = \left[ \frac{d_{\gamma F} - d_\gamma}{d_\gamma} \right] \dots \quad (13)$$

### **3.4.2 Inverted Optical Microscope**



Fig. 3.8: Olympus Inverted Optical Microscope.

As shown in Figure 3.8, the inverted optical microscope is used to observe the sample microstructure up to 1000x magnification. For this, the samples were prepared by mechanical grinding from 600 to 3000 grit SiC coated emery paper and then polished up to 1µm size diamond paste to obtain a mirror finish without many scratches. The samples were then chemically etched in a solution containing 2g CuCl<sub>2</sub>, 40ml HCl, and 40ml ethanol for 5mins by immersion swabbing technique. Etching is done to reveal the cast microstructure containing dendrites and grain boundaries and any secondary precipitates in micron size if available.

### 3.4.3 Field Emission Gun - Scanning Electron Microscope (FEG-SEM)

A revolution in the electron microscope was manifested by the introduction of the Field Emission Gun – Scanning Electron Microscope. This microscope offers higher magnification and resolution than the conventional SEM, capable of observing up to 500,000x magnification, unlike the conventional SEM, which can only observe up to 100,000x. Very fine features less than 50nm with good image resolution can be observed.

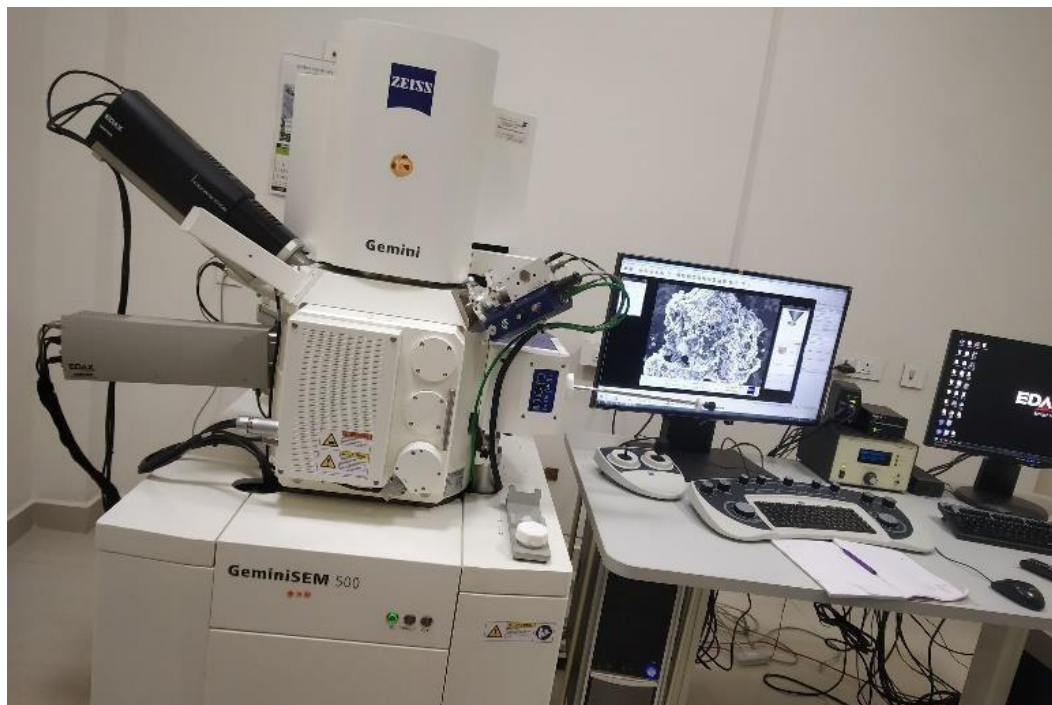


Fig. 3.9: Zeiss GeminiSEM500 FEG-SEM

The Scanning Electron Microscopy characterization for dual-phase  $\gamma/\gamma'$  microstructure in the as-cast and heat-treated samples were done using Zeiss GeminiSEM500 FE-SEM (Figure 3.9). The samples taken for observation were electropolished using 10% perchloric acid in ethanol under 20V DC for 3mins at -10°C temperature. The electropolished samples were then observed

at high magnification using the In-lens FE-SEM with an aperture size of 20 $\mu$ m and electron accelerating voltage of 2kV. The working distance for the observation was kept at less than 5mm for better quality images. The In-lens FE-SEM can produce high-quality images with spatial resolution down to 0.6nm. It uses low voltages and avoids the electrical charging of the samples. Elemental quantification was done using the EDS detector integrated into the microscope.

### 3.5 Mechanical Characterization

#### Vickers Microhardness Tester



Fig 3.10: UHL VHMT Vickers Microhardness Tester.

Vickers Microhardness Test makes use of the square pyramidal diamond indenter for every kind of material. It is easier to use than any other hardness testing instrument as the required calculations are independent of the size of the indenter. This hardness test is usually used for smaller-sized materials where lower loads are applied for hardness measurement. However, the loads applied to vary from 1 to 120kg, but most hardness measurements are up to a maximum of 50kg. (Figure 3.10)

The hardness measurement is given by the formula,

$$HV = 0.1891 \left( \frac{F}{d^2} \right) \text{ GPa} \dots \dots \dots \quad (14)$$

where,

$F$  = applied load (in N)

d = average of the diagonal length of the square pyramid (in mm)

Good surface preparation with minimal surface roughness is required for accurate hardness measurement, as the load applied in this type is less compared to other hardness testers.

## Chapter 4

# RESULTS AND DISCUSSION

### 4.1 As-cast alloys.

#### 4.1.1 Microstructure of as-cast alloys

The images in Figure 4.1 show the optical images of the as-cast alloys revealing dendritic microstructure. The microstructure shows both the dendritic and solute-rich inter-dendritic regions. It was observed that with an increase in %Cr, the microstructure was refined, as it is evident from the reduced secondary dendritic arm spacing.

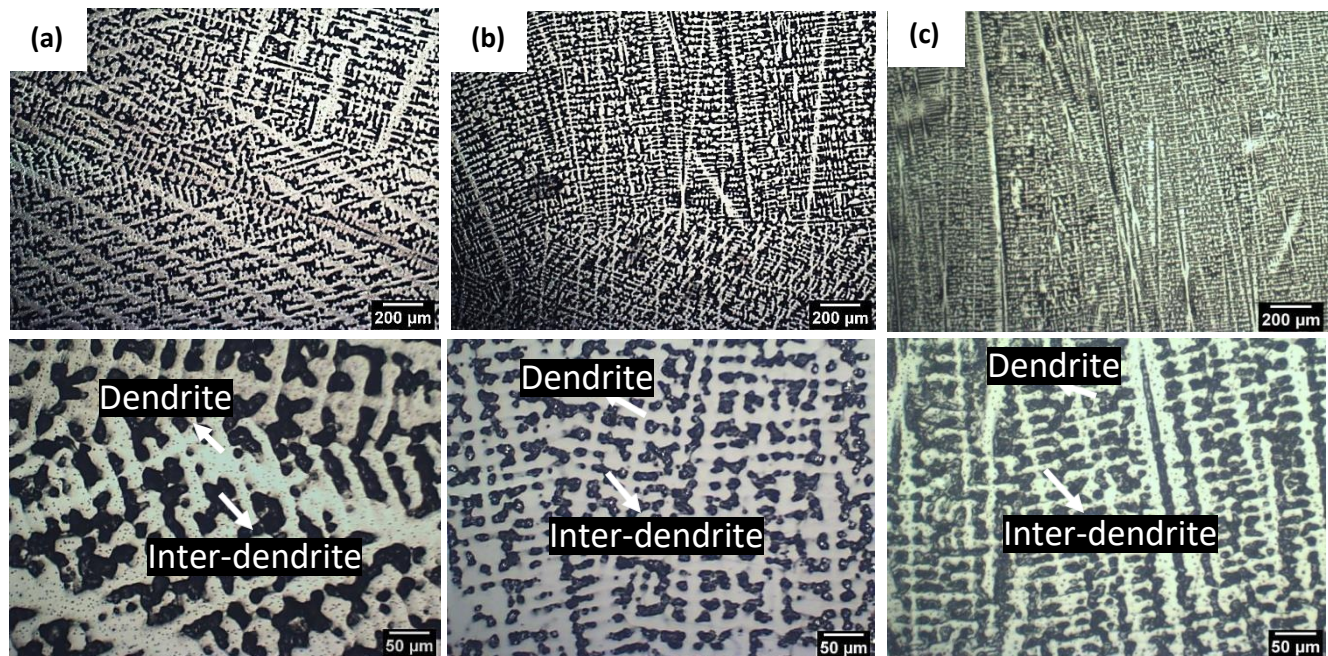


Fig. 4.1: Inverted Optical images of as-cast alloys (a) A1-0 at.%Cr, (b) A2-10 at.%Cr, (c) A3-20 at.%Cr.

Table 4.1: EDS elemental composition (in at.%) of the bulk material and in dendritic (D) and inter-dendritic regions (ID) of as-cast alloys A1-0 at.%Cr, A2-10 at.%Cr, A3-20 at.%Cr

Elements	A1 – 0at.%Cr			A2 – 10at.%Cr			A3 – 20at.%Cr		
	D	ID	Bulk	D	ID	Bulk	D	ID	Bulk
<b>Co</b>	61.99	59.09	60.16	52.58	46.20	50.49	51.77	48.42	49.57
<b>Ni</b>	26.52	27.46	27.35	26.27	28.83	27.75	16.10	18.50	18.39
<b>Al</b>	4.39	3.17	4.01	3.06	1.98	3.37	3.28	3.42	3.58
<b>Ti</b>	7.11	10.28	8.48	5.71	15.36	8.28	5.44	13.08	8.87
<b>Cr</b>	0	0	0	12.37	7.63	10.11	23.40	16.58	20.64
<b>Total</b>	<b>100</b>			<b>100</b>			<b>100</b>		

#### 4.1.2 EDAX – EDS Analysis

The elemental composition shown in Table. 4.1 compares the individual elements in the dendritic and inter-dendritic regions to the bulk composition. The segregation of the elements in the respective dendritic and inter-dendritic regions affects the formation and size of  $\gamma'$  in those regions.

Figure 4.2 shows the EDS line scan analysis for all three alloy compositions show variation in the elemental composition of the dendrite and inter-dendritic region. In all three compositions, there is a depletion of Cr and an increase in Al and Ti in the inter-dendritic zones.

It is found that with increased Cr content in the alloys, the diffusion of Ti in the inter-dendrite is sharper in the 20 at.% Cr compared to 0 at.% Cr. Furthermore, a sharp drop in the Cr content in the inter-dendritic zone is observed with increased Cr content from 0at.% Cr to 20at.% Cr. As Cr goes into solid solution in the  $\gamma$  matrix, diffusion of Cr into the dendritic region occurs in alloys with increasing Cr content resulting in the Co depletion from the dendritic to inter-dendritic region. This observation infers that Cr partitions some Co into inter-dendrite to promote the formation of  $\gamma'$  -  $(\text{Co}, \text{Ni})_3(\text{Al}, \text{Ti})$  in the inter-dendritic region while decreasing the Co content in the  $\gamma'$  in the dendrites. Diffusion of alloying elements in the inter-dendritic region promotes coarser  $\gamma'$  in the inter-dendrites compared to dendrites. The images shown in Figure 4.3 reveal the variation in the  $\gamma'$  precipitate size in the dendritic and inter-dendritic regions in the as-cast structure.

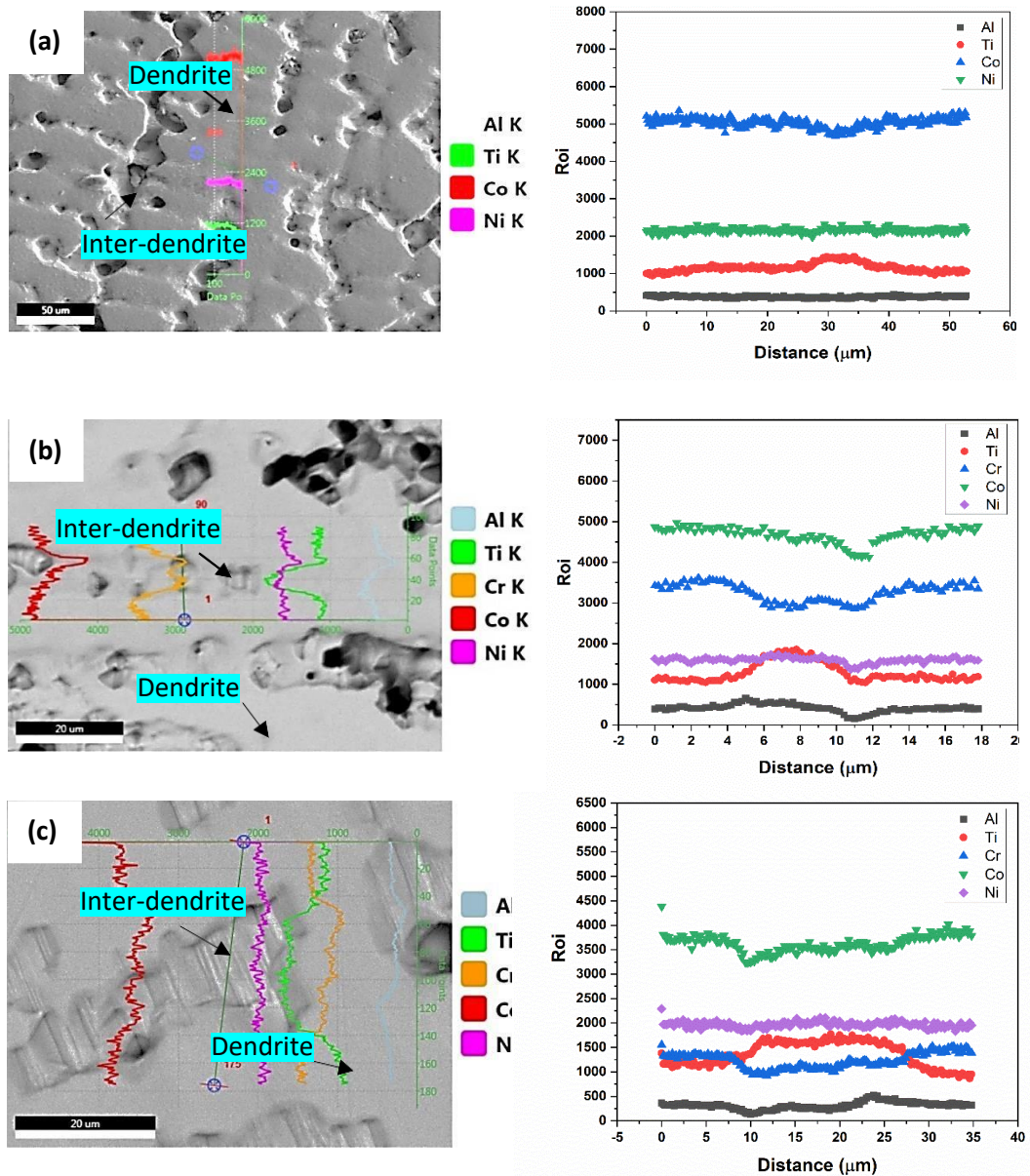


Fig. 4.2: Line scan of as-cast alloys (a) A1-0 at.%Cr, (b) A2-10 at.%Cr, (c) A3-20 at.%Cr

#### 4.1.3 Scanning Electron Microscopic (SEM) Images

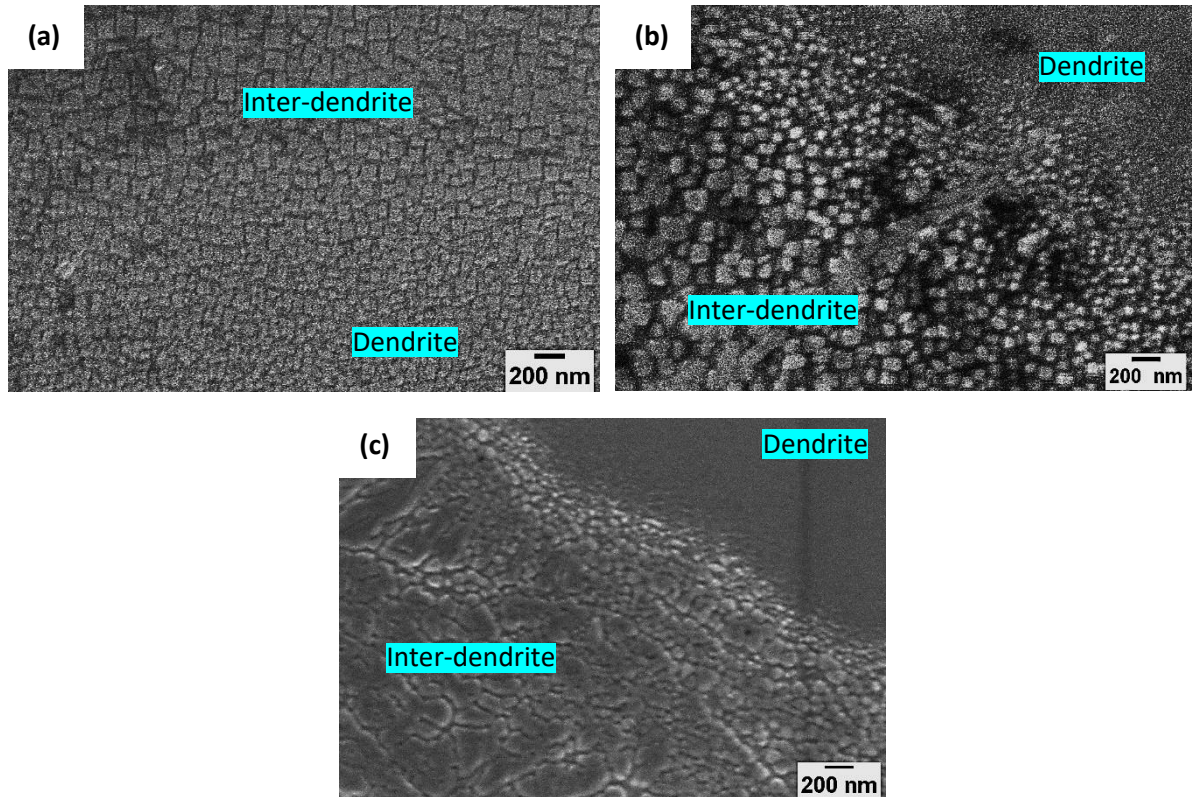


Fig. 4.3: SEM images of as-cast alloys (a) A1-0 at.%Cr, (b) A2-10 at.%Cr and (c) A3-20 at.%Cr.

Ti enrichment in the inter-dendritic region caused the coarsening of  $\gamma'$  in the cast structure, as seen in Figure 4.3 (a), (b), and (c). As Ti is a strong  $\gamma'$  strengthener, it substitutes Al thereby influencing the APB and lattice misfit between  $\gamma/\gamma'$  interface [19-20]. Coarsening causes coalescence of  $\gamma'$  precipitates, thereby increasing the inter-particle distance while decreasing the volume fraction. Some researchers have also reported an increased volume fraction of  $\gamma'$  due to increased coalescence, but the number density decreases. [19-20] This results in high hardness, but lower strength at high temperatures as the  $\gamma'$  is not uniform and unstable at high temperatures.

The  $\gamma'$  precipitate size varies from 30nm in the dendritic region to 105nm in the inter-dendritic region. Coarser  $\gamma'$ , having a size greater than 105nm, is also present in some cast alloys with an irregular and elongated shape. This is caused due to non-uniform solidification in various zones of the cast alloy. In order to remove the inhomogeneity in the cast microstructure, these samples are heat-treated above the solvus temperature to form a uniform isotropic microstructure.

#### 4.2 Differential Scanning Calorimetry (DSC) Studies

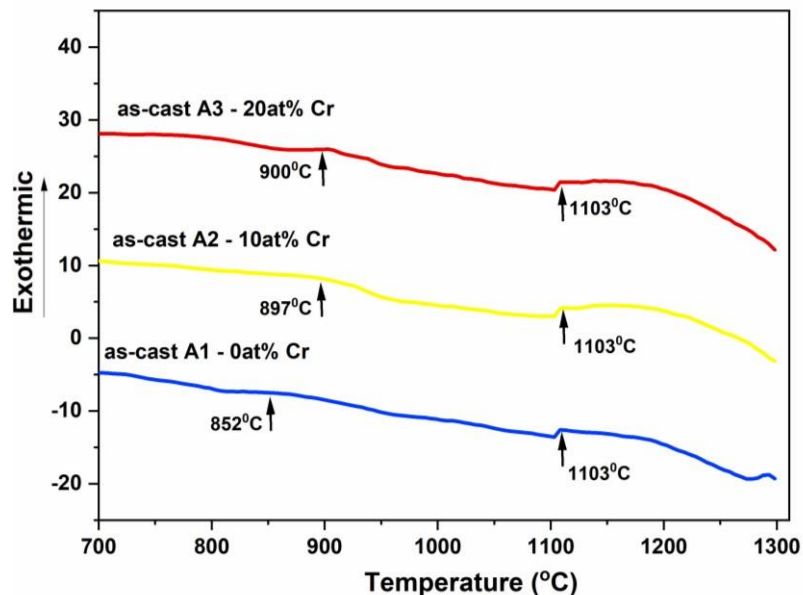


Fig. 4.4: DSC results of as-cast alloys A1-0 at.%Cr, A2-10 at.%Cr and A3-20 at.%Cr.

DSC measurements were performed to study the phase transformation temperatures of these alloys and are shown in Figure 4.4. The stability of the  $\gamma'$  phase is higher with increasing in %Cr as the dissolution temperature keeps rising from 852°C to 900°C. In contrast, the solvus temperature above which the FCC phase is stable did not change with an increase in the %Cr content, i.e., 1103°C.

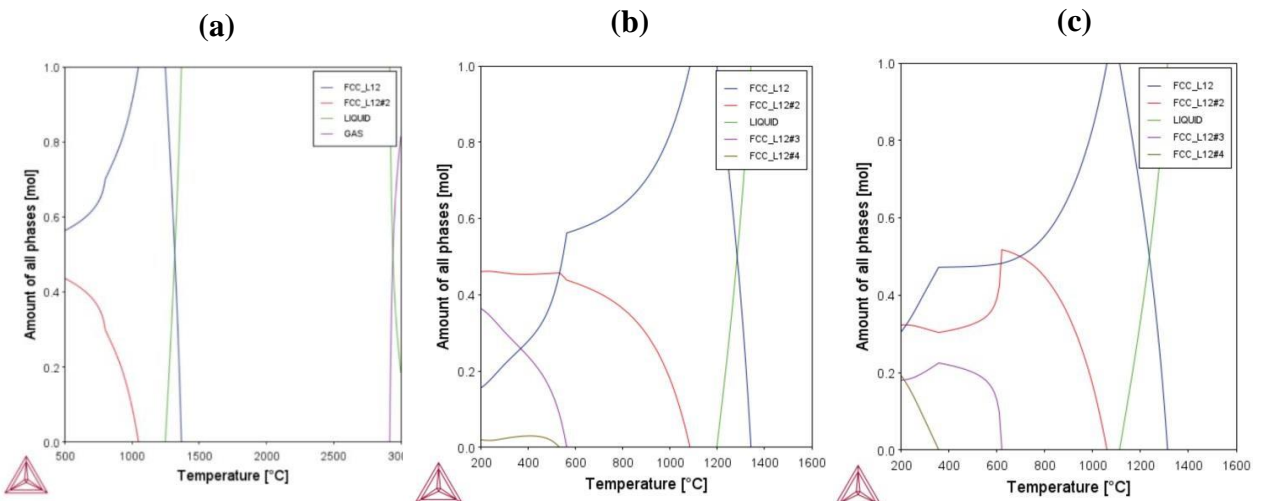


Fig. 4.5: ThermoCalc results of as-cast alloys (a) A1-0 at.%Cr, (b) A2-10 at.%Cr and (c) A3-20 at.%Cr.

ThermoCalc results also reveal the presence of FCC\_L1<sub>2</sub> as the  $\gamma$  matrix phase and FCC\_L1<sub>2</sub>#2 as the ordered  $\gamma'$  phase taken from the ThermoCalc TCNI8 database.

### **4.3 X-Ray Diffraction Analysis**

The XRD measurements were taken for the as-cast and as-solutionized samples to understand the phase evolution and correlate the lattice parameter changes before and after the heat treatment. The lattice parameter 'a' in 'Å' is measured using the Bragg's Law given as,

where,

$\lambda$  – wavelength of source taken (Cu- $\text{k}\alpha$  = 1.5406 Å)

d – lattice spacing (in Å)

*a* – lattice parameter (in Å)

$h, k, l$  – miller indices of crystal planes

The XRD data of all three as-cast alloys shown in Figure 4.6 reveal the presence of FCC crystal structure for the major and minor phases with the lattice indices as (111), (200), (220), (311), and (222).  $\gamma'$ , having an ordered FCC crystal structure, show overlapping peaks with the  $\gamma$  – matrix phase and hence had to be deconvoluted to separate the individual peaks of  $\gamma$  and  $\gamma'$ . The deconvolution is carried out for all the heat-treated alloys to evaluate the lattice mismatch between  $\gamma$  and  $\gamma'$  with change in the heat-treatment method.

The unindexed peak is indicated as ‘?’ and can be predicted to be generated due to background noise as no secondary phase other than  $\gamma'$  was observed in the SEM images.

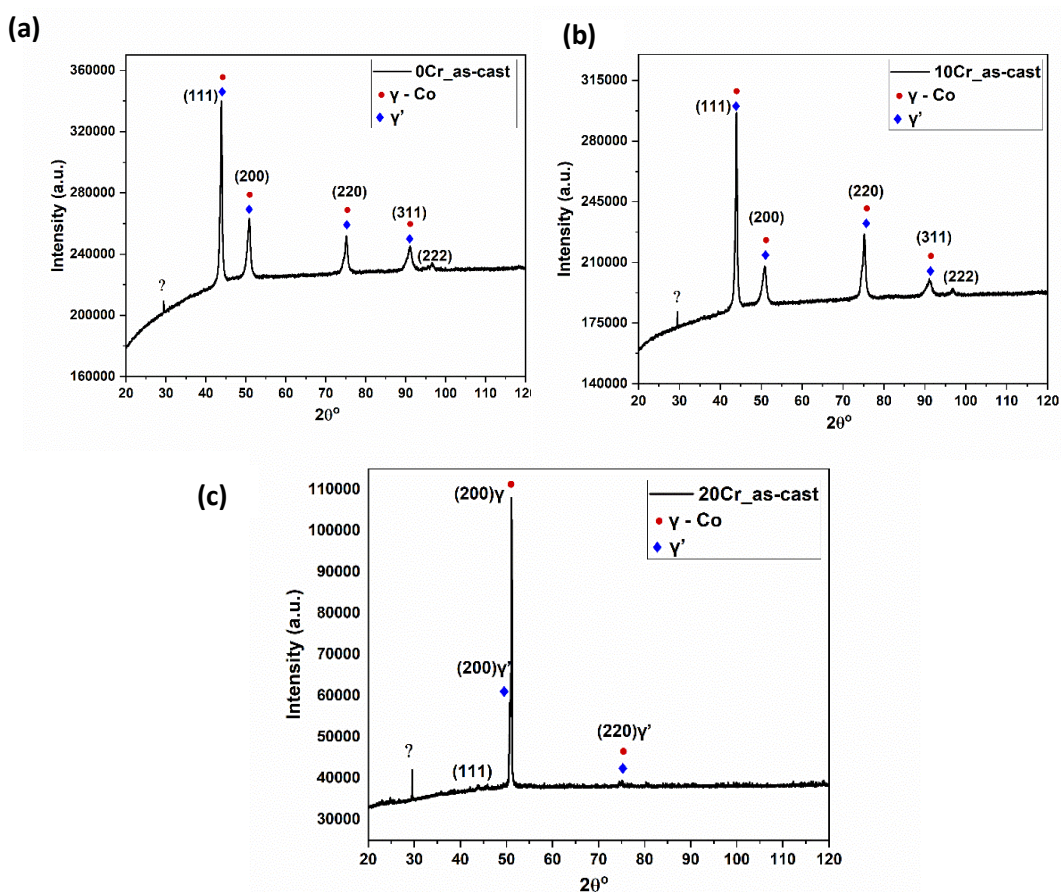


Fig. 4.6: XRD plots of as-cast alloys (a) A1-0 at.%Cr, (b) A2-10 at.%Cr and (c) A3-20 at.%Cr showing FCC crystal structure.

#### 4.4 As-solutionized samples

The as-cast samples were then heat-treated at 1150°C and 1200°C and cooled using various cooling methods like WQ, AC, and FC to study the precipitate evolution in different cooling conditions in terms of precipitate size, precipitate shape, lattice misfit across matrix and precipitate and correlate with the hardness data.

##### 4.4.1 Field Emission – Scanning Electron Microscope (FE-SEM)

Figure 4.7 shows the SEM images of the alloys heat-treated at 1150°C, and Figure 4.10 shows the SEM images of the alloys heat-treated at 1200°C. The images reveal the formation of precipitates in all the solutionized alloys cooled at different cooling rates. These precipitates are referred to as ‘cooling precipitates’ and thus are formed during cooling.

###### 4.4.1.1 Solutionization at 1150°C

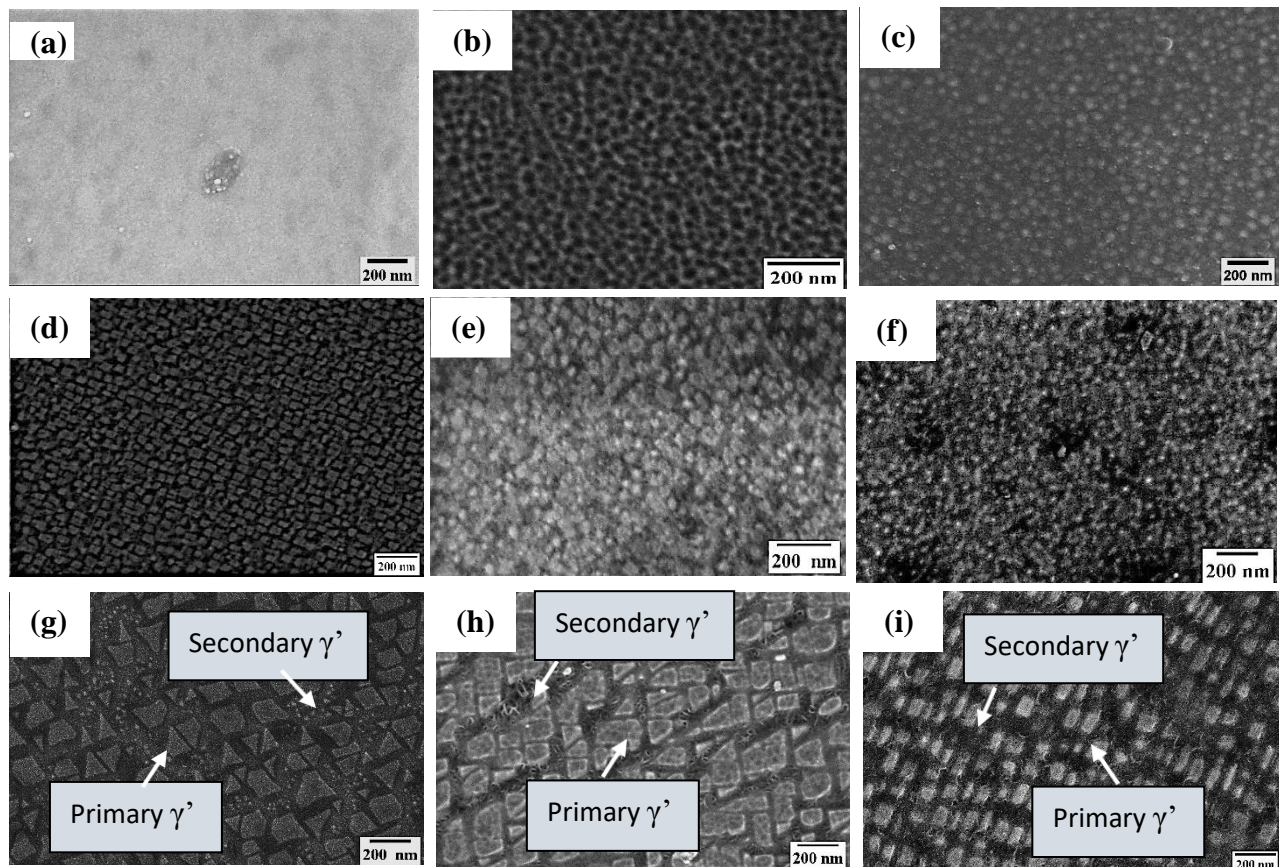


Fig. 4.7: SEM images of  $\gamma/\gamma'$  microstructure of alloys heat treated at 1150°C followed by (a)-(c) WQ, (d)-(f) AC, (g)-(i) FC; (a)-(g) 0at.% Cr, (b)-(h) 10at.% Cr, (c)-(i) 20at.% Cr.

The above images show the as-cast samples heat-treated at  $1500^{\circ}\text{C}$ . A uniformly distributed finer  $\gamma'$  precipitates with sizes varying from 20nm to 35nm is found in the WQ and AC samples, as shown by the histogram in Figure 4.8. In contrast, the bimodal size distribution of  $\gamma'$  is found in FC samples with primary  $\gamma'$  size. 63nm to 113nm as seen from the histogram in Figure 4.9.

An increase in %Cr among the alloys changes the  $\gamma'$  shape from cuboidal having sharp corners to rounded cuboidal shapes observed for alloys cooled by WQ and AC. These results are consistent with the results obtained by Tianyou Wang et al. [8] and Shaik Adil et al. [21]. However, alloys cooled by FC retain the cuboidal shape for all alloy compositions, showing a higher lattice mismatch than the WQ and AC samples. The transformation to a spherical shape is due to a decrease in the lattice misfit and an increase in the lattice parameter of  $\gamma$  which also matches with the results obtained by some researchers [14-15]. This is due to the enrichment of Cr in the matrix phase that replaces Co or Ni from the matrix phase.

#### 4.4.1.2 Particle size distribution curve

##### i. Solutionization at $1150^{\circ}\text{C}$ , AC

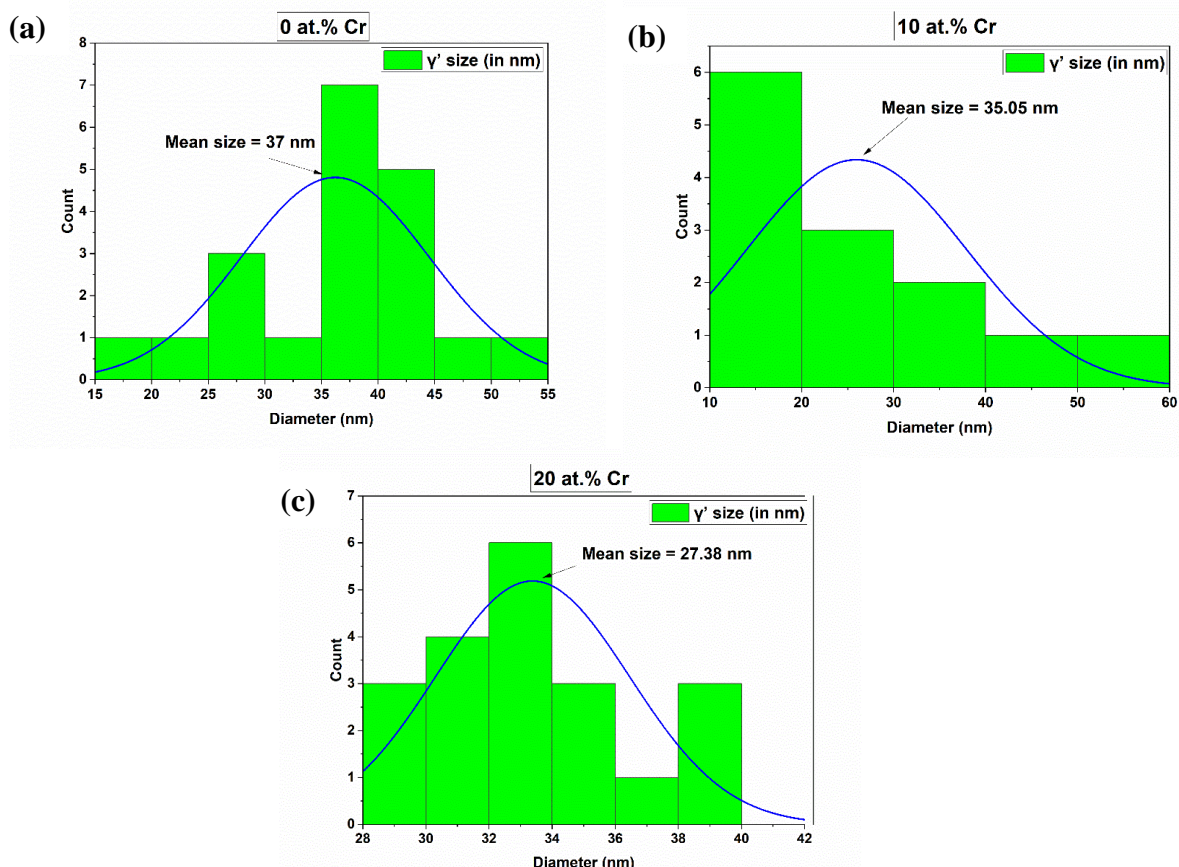


Fig. 4.8: Histograms showing a unimodal size distribution of  $\gamma'$  for the alloys (a) 0at.% Cr, (b) 10at.% Cr, (c) 20at.% Cr heat-treated at  $1150^{\circ}\text{C}$  and AC

The particle size distribution curve shown in Figure 4.8 is for the samples heat-treated at 1150°C and AC. The graphs correlate with the SEM images in Figure 4.7 showing a unimodal size distribution of  $\gamma'$  with a decrease in the average particle size and increased Cr content. Particle size is found to be ranging from 27nm to 37nm with decreasing pattern from 0at.% Cr to 20at.% Cr. These are consistent results obtained by K.A. Christofidou et al. [14], where the  $\gamma'$  size is less than 50nm.

The SEM images in Figure 4.7, reveal a bimodal particle size distribution for the alloys furnace cooled post solutionization at 1150°C. This is quantitatively seen in the histogram in Figure 4.9.

The effect of Cr on the  $\gamma'$  size is still unclear and can be understood from APT (Atomic Probe Tomography) results showing the partitioning of Cr in  $\gamma$  and  $\gamma'$  phases.

## ii. Solutionization at 1150°C, FC

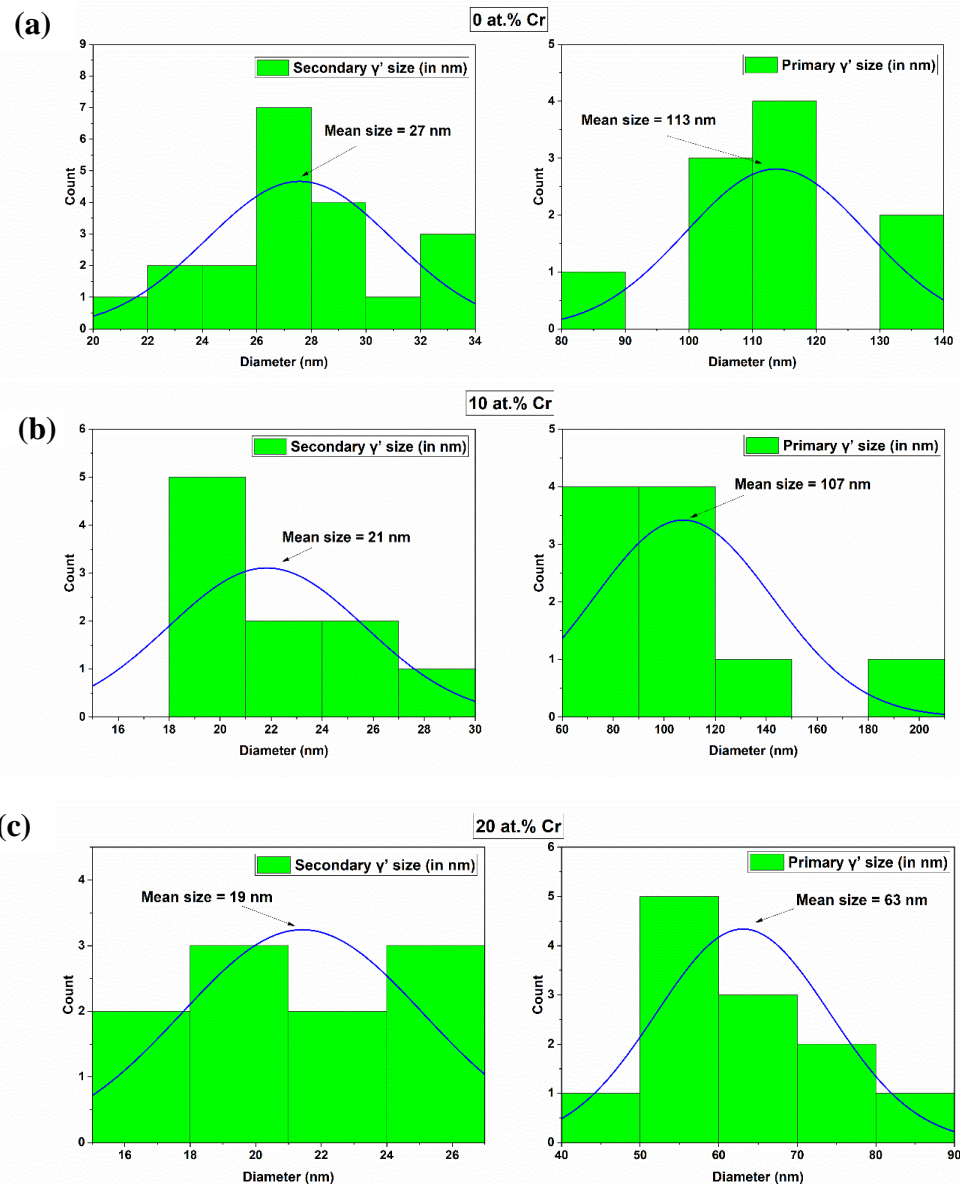


Fig. 4.9: Histograms showing a bimodal size distribution of  $\gamma'$  for the alloys (a) 0at.% Cr, (b) 10at.% Cr, (c) 20at.% Cr heat-treated at 1150°C and FC

Bimodal size distribution is evident for the alloys that are FC [9-11] due to the effect of slow cooling which gives enough time for the diffusion and coalescence of  $\gamma'$  forming coarser primary and finer secondary  $\gamma'$  precipitates [11-12] and [18].

#### 4.4.1.3 Solutionization at 1200°C

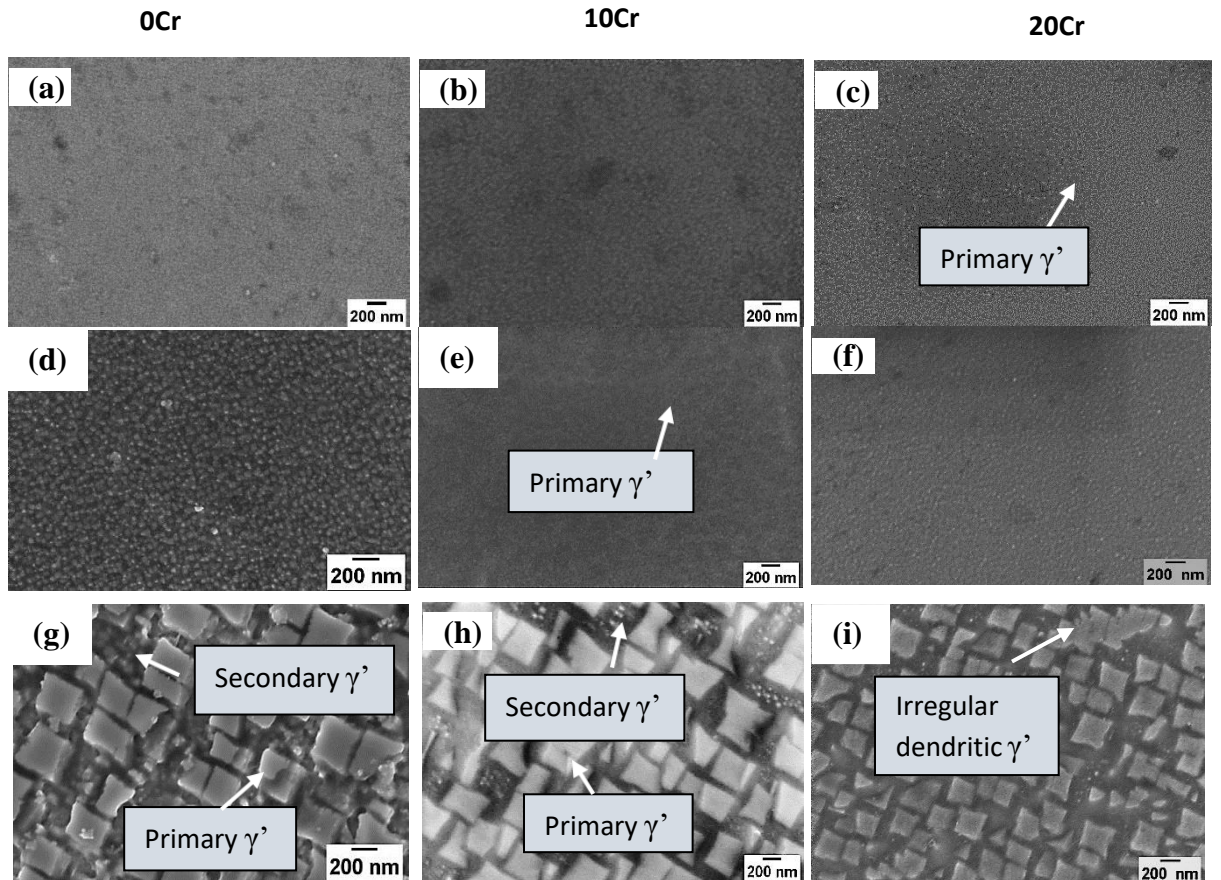


Fig. 4.10: SEM images of  $\gamma/\gamma'$  microstructure of alloys heat treated at 1200°C followed by (a)-(c) WQ, (d)-(f) AC, (g)-(i) FC; (a)-(g) 0at.% Cr, (b)-(h) 10at.% Cr, (c)-(i) 20at.% Cr.

The images in Figure 4.10 reveal cuboidal  $\gamma'$  formed in all three alloy compositions under the three-cooling conditions when solutionized at 1200°C. The effect of Cr on the  $\gamma'$  shape is not well noticed, but a size difference in the  $\gamma'$  is observed with an increase in %Cr. For WQ samples, the  $\gamma'$  size is presumed to be increasing with an increased Cr content, while for AC and FC samples, the  $\gamma'$  is decreasing. The  $\gamma'$  size distribution plots, as shown in Figure 4.11 show a unimodal size distribution of  $\gamma'$  for AC samples, while a bi-modal size distribution of  $\gamma'$  for FC samples, as seen in Figure 4.12. Bimodal size distribution in FC samples is because of the formation of secondary  $\gamma'$  precipitates formed within the  $\gamma$  channels. This observation is done for alloys heat-treated at both 1150°C and 1200°C.

#### 4.4.1.4 Particle size distribution curve

##### i. Solutionization at 1200°C, AC

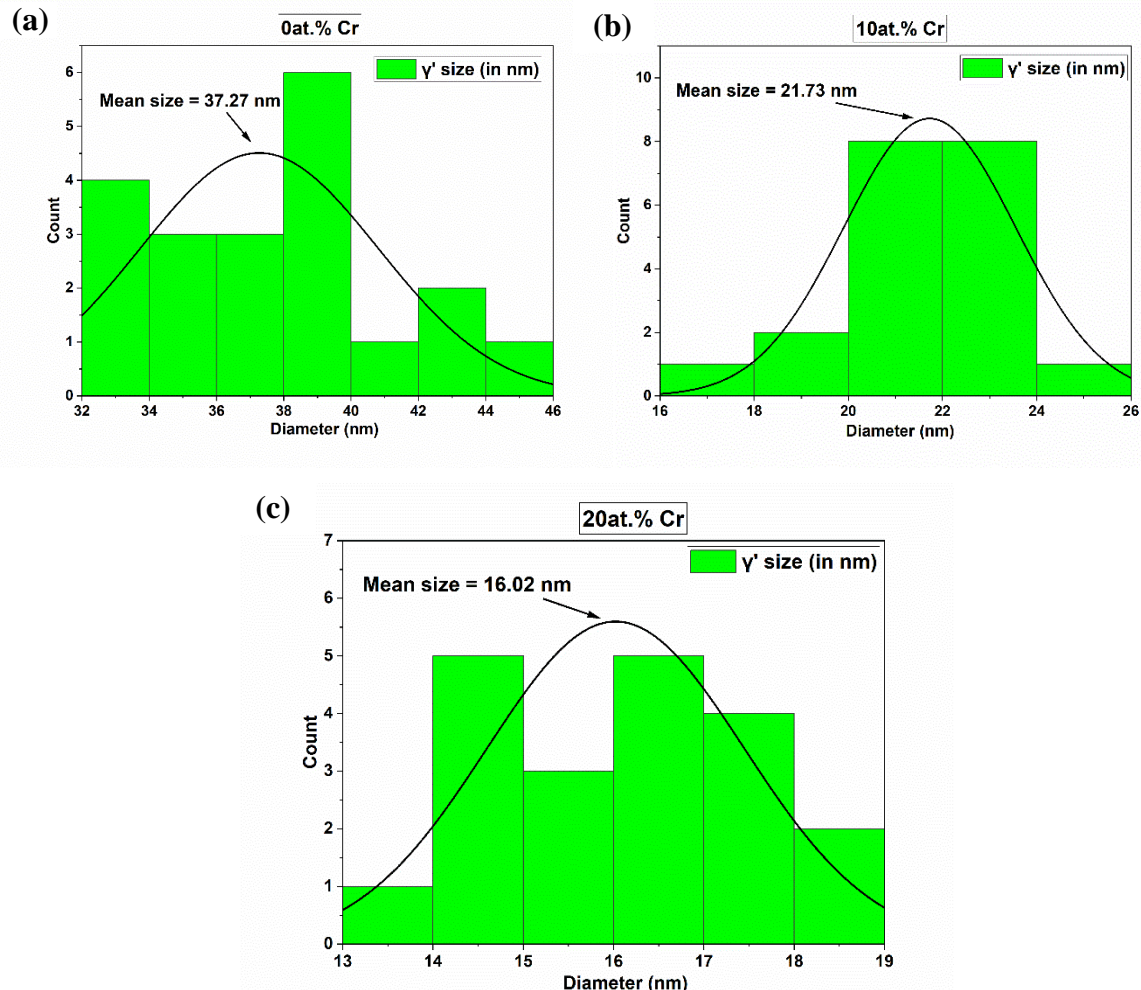
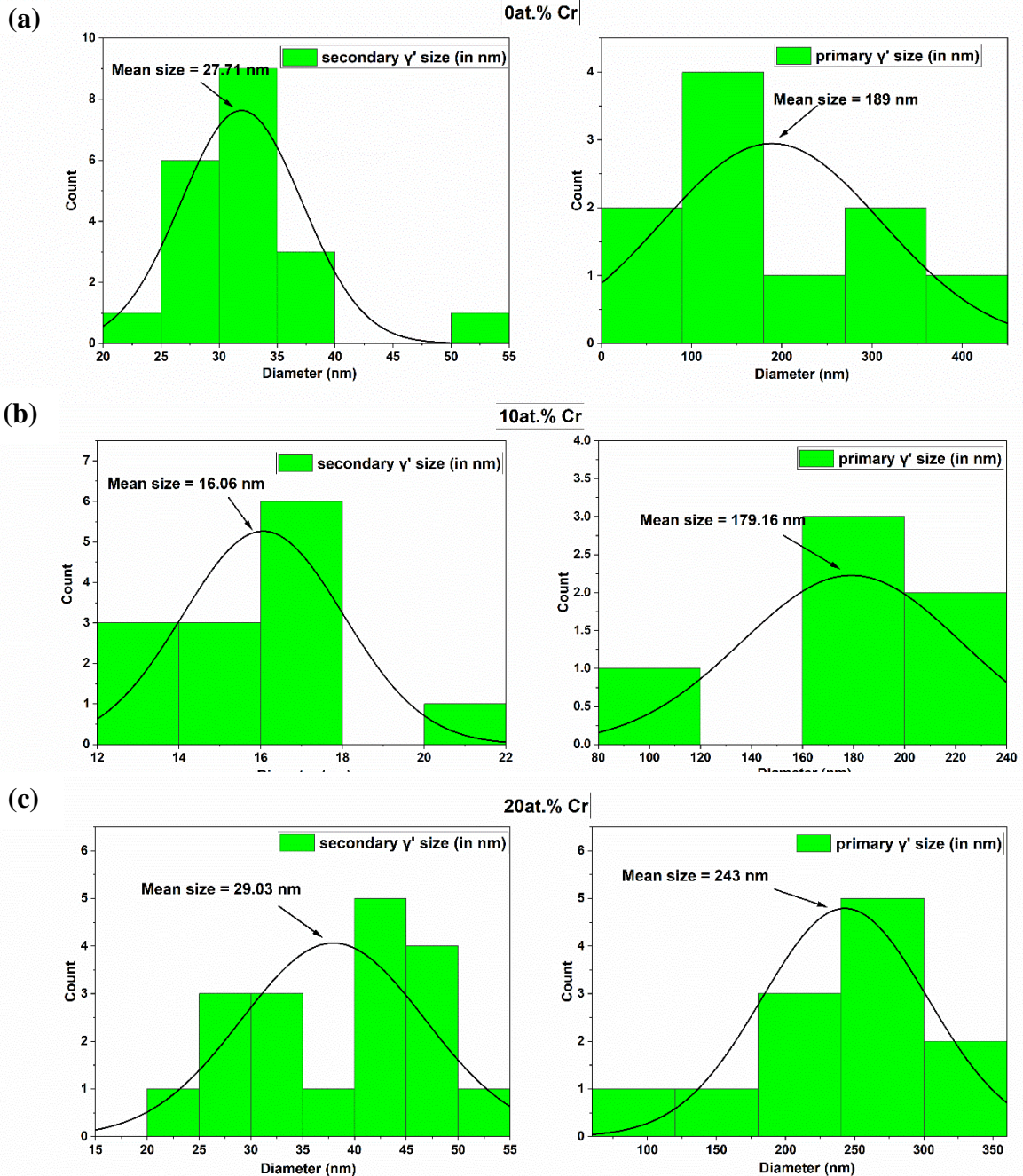


Fig. 4.11: Histograms showing a bimodal size distribution of  $\gamma'$  for the alloys (a) 0at.% Cr, (b) 10at.% Cr, (c) 20at.% Cr heat-treated at 1200°C and AC

Increasing the solutionization temperature to 1200°C, provides more driving force for the nucleation and hence influences the formation of finer  $\gamma'$  during cooling. This observation can be made for the alloys that are cooled by WQ or AC and is evident from the histogram in Figure 4.11. However, alloys cooled by FC show a varied trend where the  $\gamma'$  size follows a decreasing size pattern up to 10at.% Cr but increases with %Cr more than 10at.%. The size distribution curve for the alloys that are FC is shown in the histogram in Figure 4.12.

## ii. Solutionization at 1200°C, FC



of precipitates is controlled by the temperature difference from its solvus temperature. Thus, as seen for the alloys heat-treated at 1200°C, the volume fraction is large compared to the alloys heat treated at 1150°C due to higher temperature difference and higher driving force for nucleation.

The elastic strain energy is proportional to the precipitate volume and forms anisotropic precipitate shapes like cubes, octocubes, octodendrites, or dendrites. This is because with increased precipitate size,  $\gamma'$  loses its coherency and attains irregular morphology. Figure 4.13, Figure 4.14, and Figure 4.15 compare particle evolution under various cooling mediums. The results show quasi-spherical rounded cuboids for the WQ samples, while a more cubic morphology is observed for AC and FC samples. Thus, it is clear that the elastic strain energy dominates  $\gamma'$  evolution with a decrease in the cooling rate. Elastic strain energy also depends on the lattice mismatch between  $\gamma$  and  $\gamma'$ . Hence, with a decrease in the cooling rate, the lattice mismatch is found to be more for AC and FC samples, which gives the cubic morphology to the precipitates compared to WQ, represented in the deconvoluted plots in Figure 4.19, Figure 4.20 and Figure 4.21.

Fine-sized  $\gamma'$  precipitates are cubic as they align along the [001] direction, resembling the cube-on-cube relation with the  $\gamma$  matrix.

## 4.5 Effect of cooling rates [Microstructural Analysis]

### 4.5.1 Water Quenching (WQ)

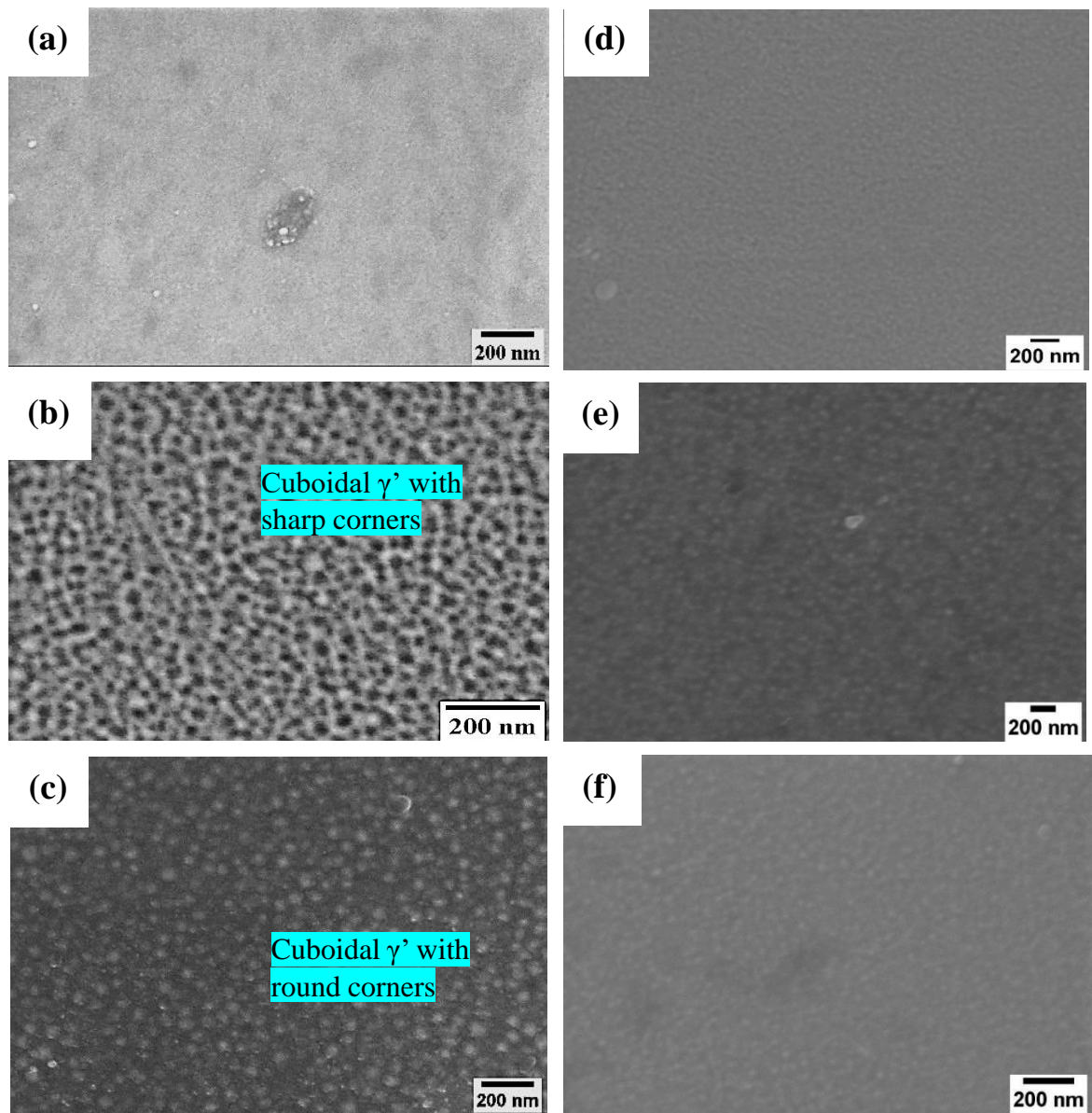


Fig. 4.13: SEM micrographs of alloys (a) 0at.% Cr, (b) 10at.% Cr and (c) 20at.% Cr heat treated at 1150°C while (d) 0at.% Cr, (e) 10at.% Cr and (f) 20at.% Cr heat-treated at 1200°C followed by WQ.

#### 4.5.2 Air Cooling (AC)

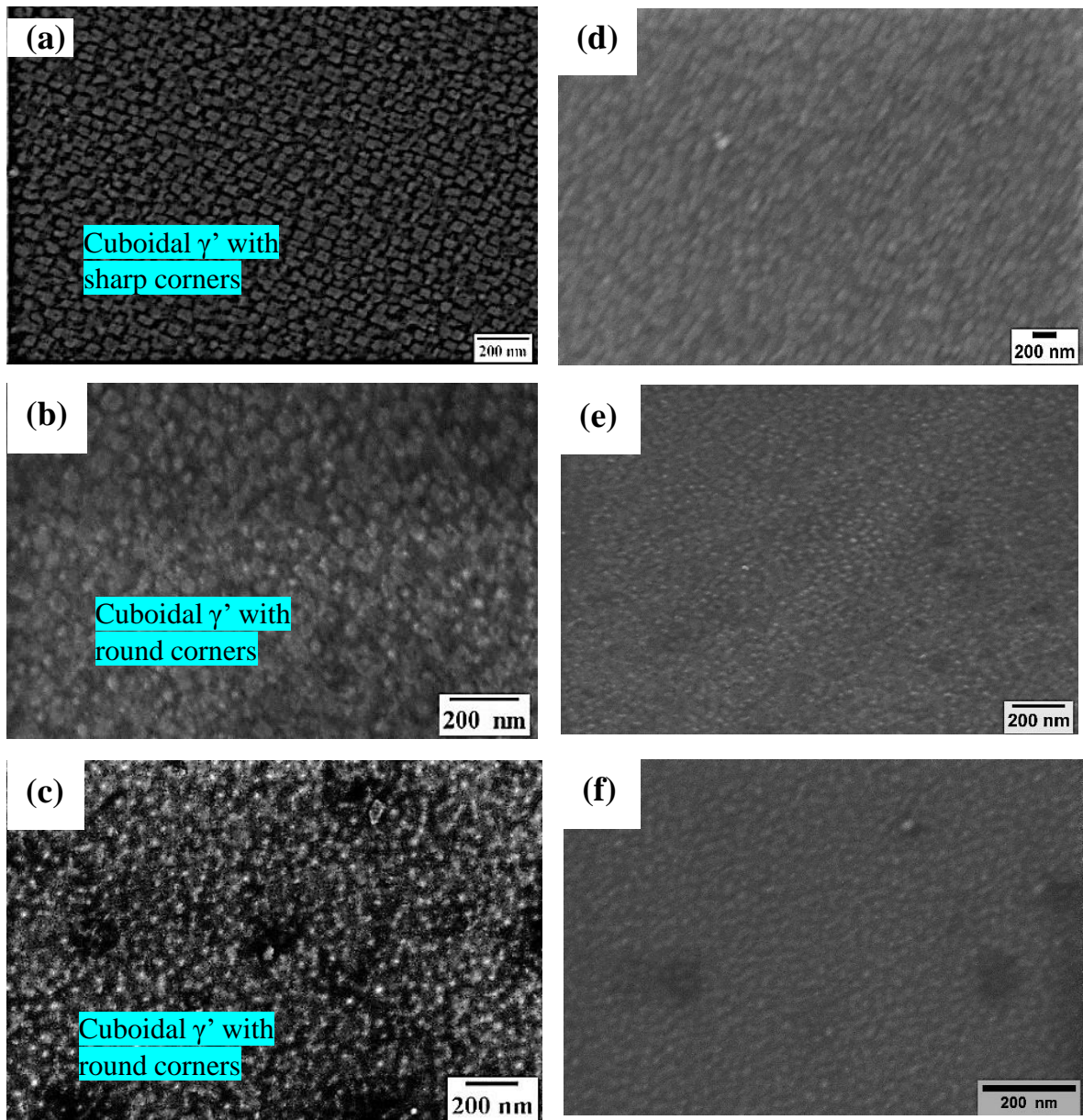


Fig. 4.14: SEM micrographs of alloys (a) 0at.% Cr, (b) 10at.% Cr and (c) 20at.% Cr heat treated at 1150°C while (d) 0at.% Cr, (e) 10at.% Cr and (f) 20at.% Cr heat-treated at 1200°C followed by AC.

#### 4.5.3 Furnace Cooling (FC)

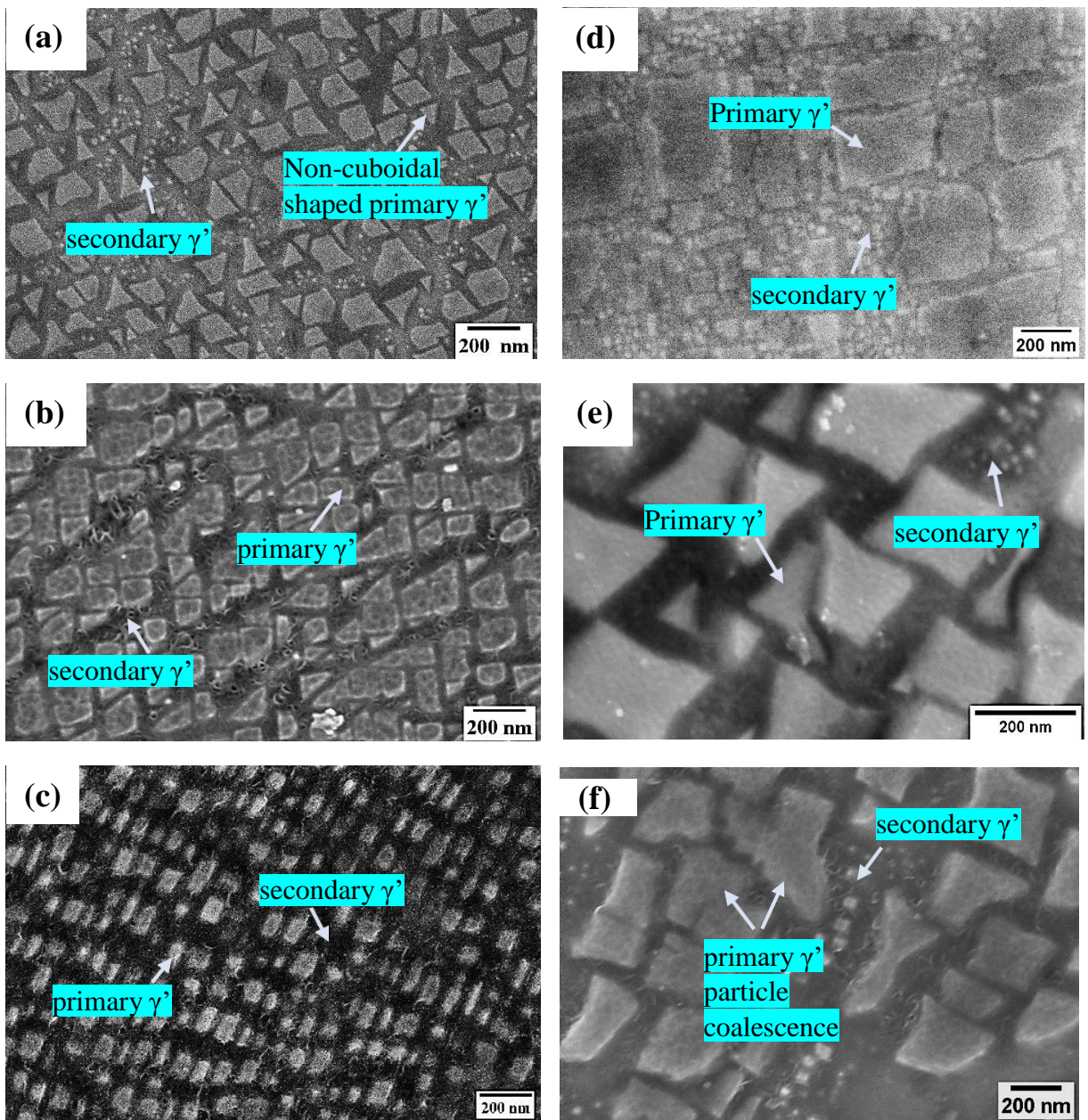


Fig. 4.15: SEM micrographs of alloys (a) 0at.% Cr, (b) 10at.% Cr and (c) 20at.% Cr heat treated at 1150°C while (d) 0at.% Cr, (e) 10at.% Cr and (f) 20at.% Cr heat-treated at 1200°C followed by FC.

Critical radius of nucleation ( $r^*$ ) of a particle related to the surface energy ( $\gamma$ ) and volume free energy ( $g$ ) is given as,

$$r^* = - \frac{2\gamma}{\Delta g} \dots \quad (17)$$

where,

$$g = \Delta h \frac{T_m - T}{T_m} \dots \dots \dots \quad (18)$$

$T_m$  = melting temperature

T = temperature of interest

$\Delta h$  = change in enthalpy

Thus, according to the equation given above that shows an inverse relationship between the critical radius of nucleation ( $r^*$ ) and the temperature difference ( $\Delta T$ ), a higher temperature difference for the heat treatment at 1200°C corresponds to a higher driving force required for the nucleation. This allows for the formation of finer particle size when heat-treated at 1200°C.

Large and coarser particle size observed in the FC samples at 1200°C as compared to 1150°C shown in Figure 4.15 is due to the samples held for a longer time at a higher temperature (1200°C). This causes the particles to nucleate first when cooled from 1200°C forming coarser primary  $\gamma'$  and the particles nucleated later form the secondary  $\gamma'$  which is finer in size than alloys cooled from 1150°C. Theoretically, a higher volume fraction of primary and secondary  $\gamma'$  is predicted to form for the samples cooled from 1150°C compared to the samples cooled from 1200°C, which can be confirmed from the results obtained by SAXS.

#### 4.6 XRD and lattice misfit measurements

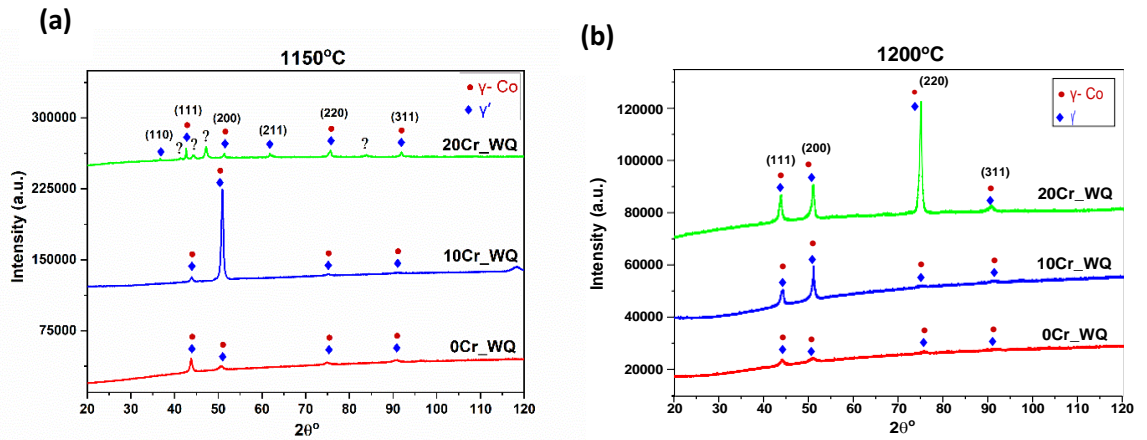


Fig. 4.16: XRD plot of samples heat-treated at (a) 1150°C - WQ and (b) 1200°C - WQ.

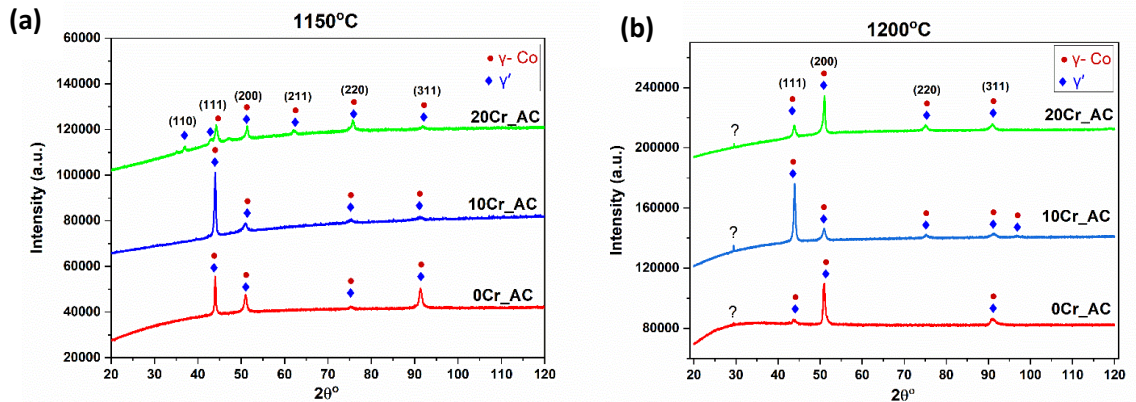


Fig. 4.17: XRD plot of samples heat-treated at (a) 1150°C - AC and (b) 1200°C - AC.

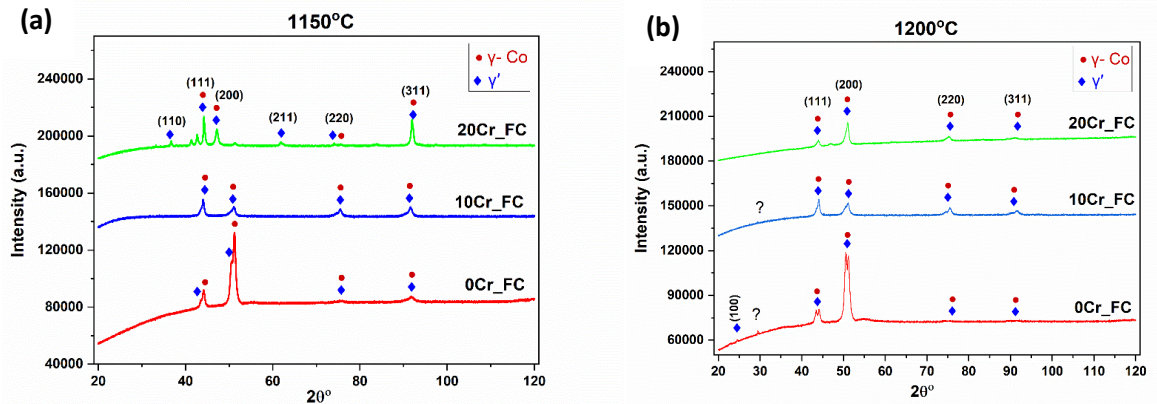


Fig. 4.18: XRD plot of samples heat-treated at (a) 1150°C - FC and (b) 1200°C - FC.

The XRD plots shown in Figure 4.16, Figure 4.17, and Figure 4.18 for alloys heat-treated at both 1150°C and 1200°C show the presence of minor  $\gamma'$  phase and major  $\gamma$ -matrix phase for all the all compositions.  $\gamma'$  superlattice peaks are distinctly observed in some heat-treated plots showing at indices of (100), (110) and (211). Remaining  $\gamma'$  peaks are overlapped with the matrix phase at the indices (111), (200), (220) and (311). These peaks corresponding to the FCC crystal structure for the  $\gamma$ -matrix phase and FCC – L1<sub>2</sub> structure for  $\gamma'$  phase resemble a coherent lattice misfit between the ordered and the disordered  $\gamma/\gamma'$  phase.

#### 4.6.1 Effect of cooling rates [XRD Analysis]

##### i. Water Quenching (WQ)

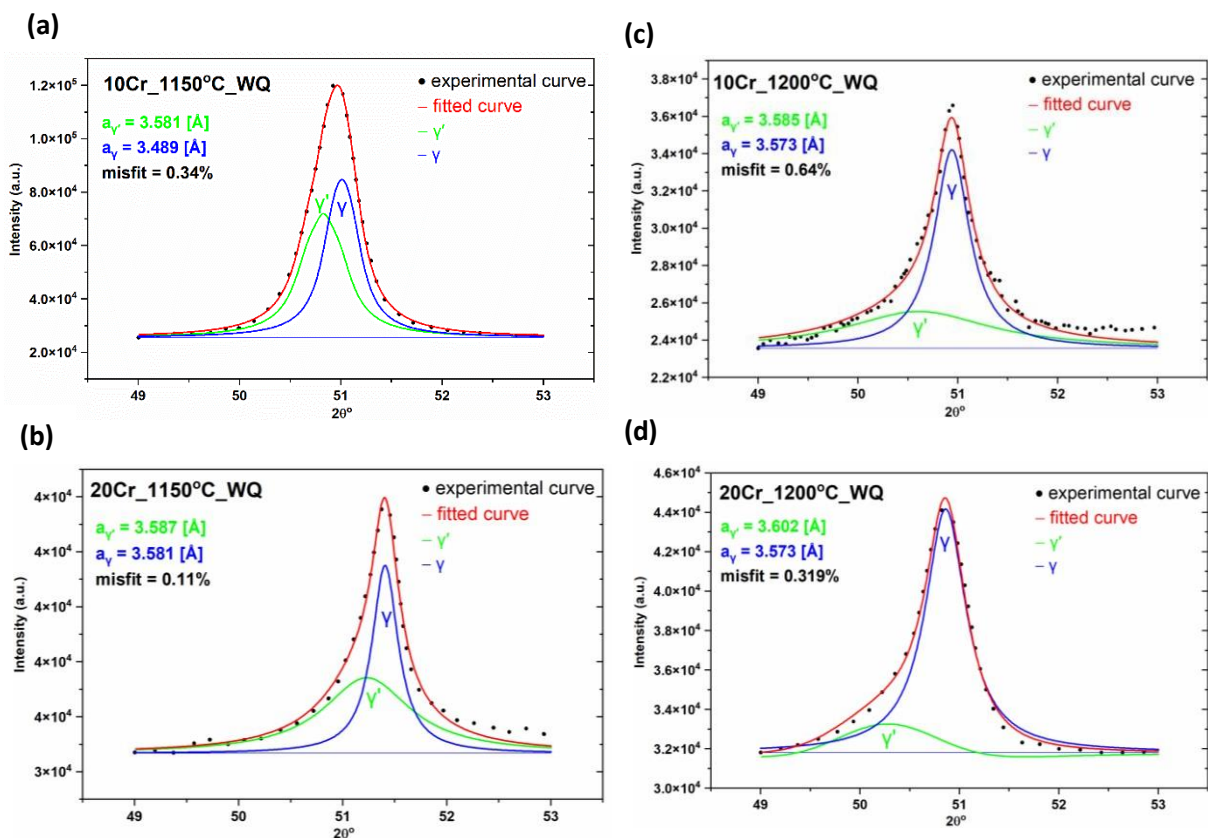


Fig. 4.19: XRD (200) deconvoluted peaks for WQ samples heat-treated at (a) 10Cr, 1150°C (b) 20Cr, 1150°C (c) 10Cr, 1200°C and (d) 20Cr, 1200°C.

Deconvolution of the peaks for the alloy containing 0at.% Cr and WQ post solutionization treatment were not possible as the overlapping peaks were not distinctly separable.

## ii. Air Cooled (AC)

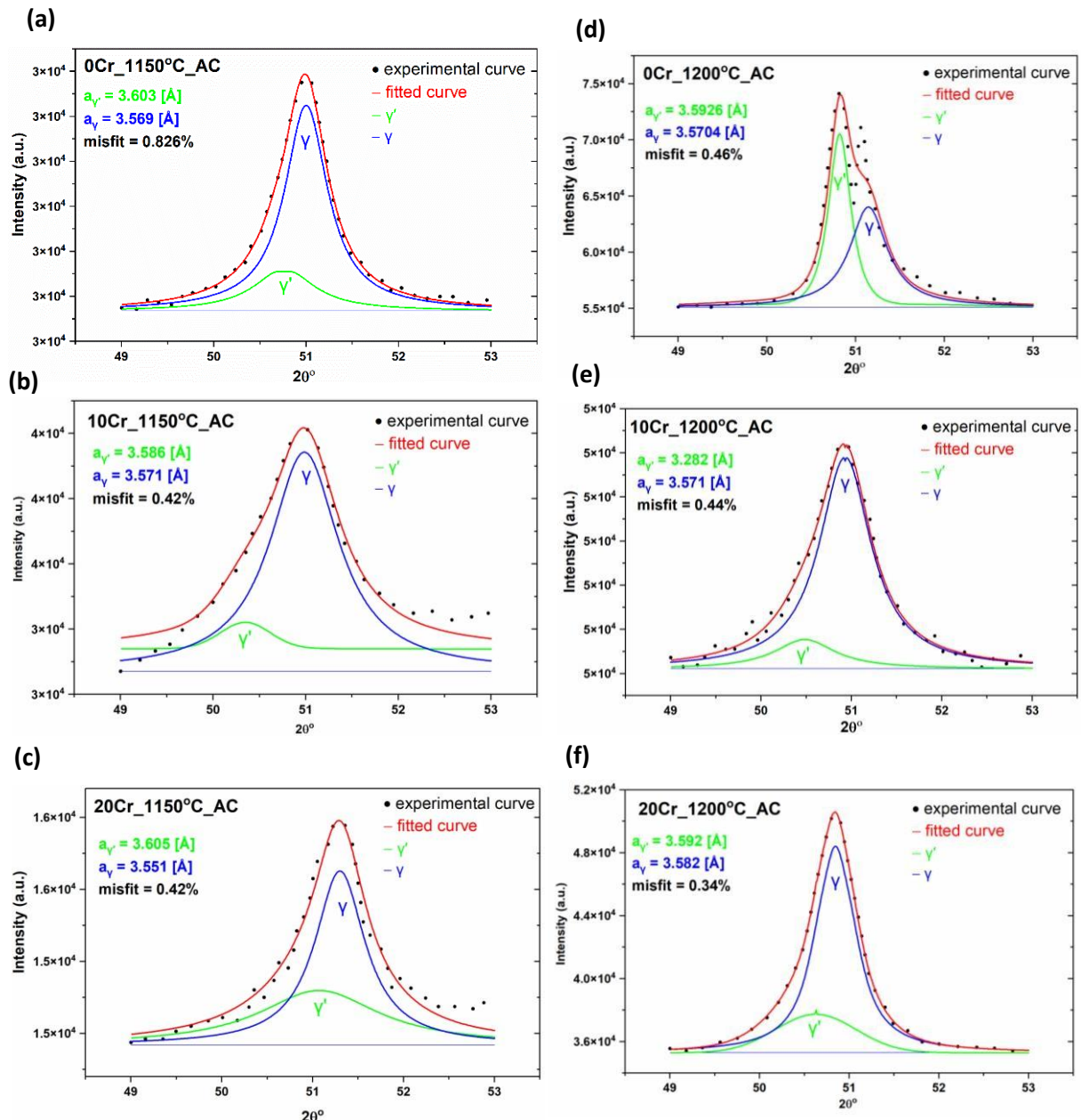


Fig. 4.20: XRD (200) deconvoluted peaks for AC samples heat-treated at (a) 0Cr, 1150°C (b) 10Cr, 1150°C (c) 20Cr, 1150°C, (d) 0Cr, 1200°C, (e) 10Cr, 1200°C and (f) 20Cr, 1200°C.

### iii. Furnace Cooled

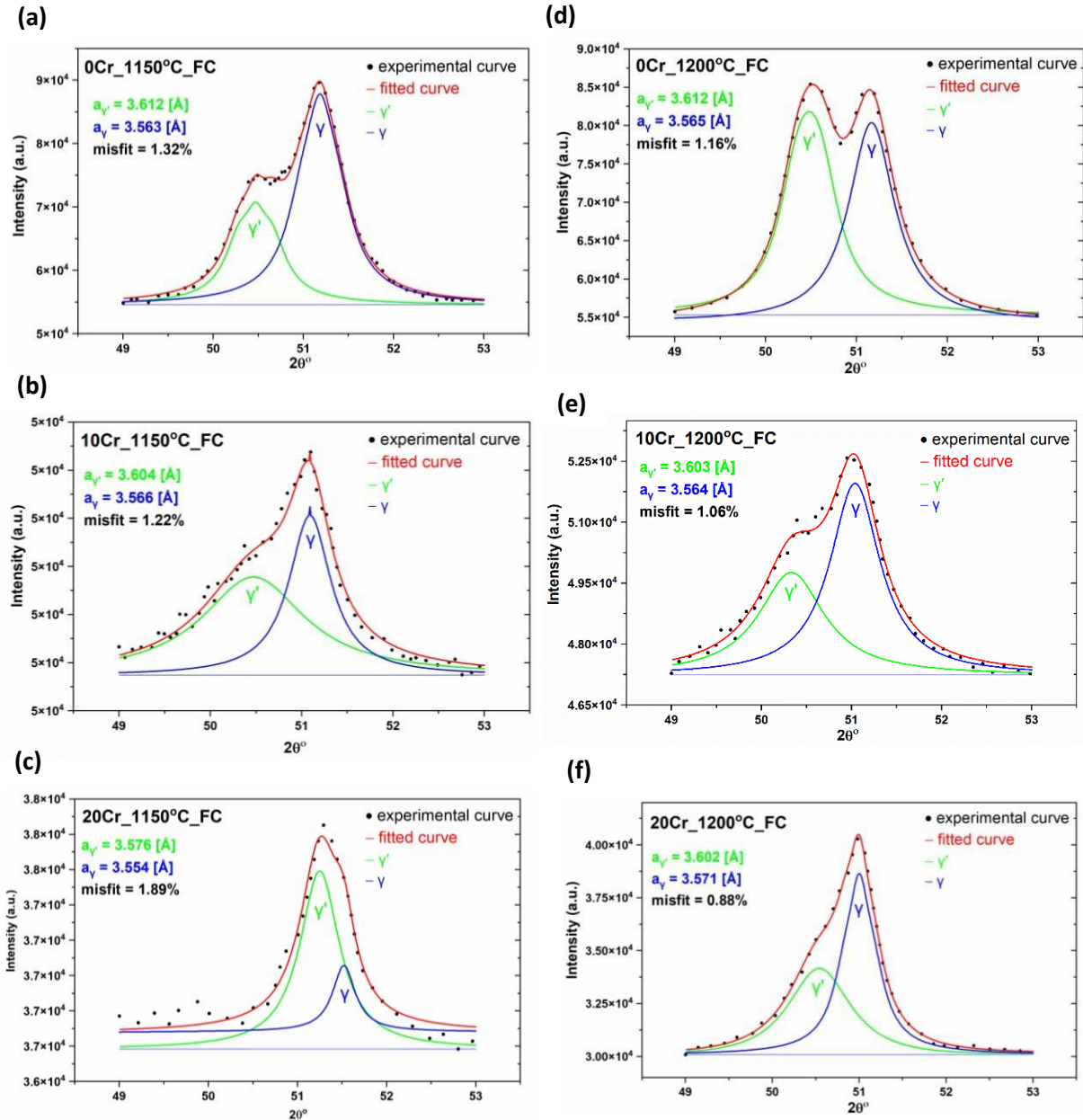


Fig. 4.21: XRD (200) deconvoluted peaks for FC samples heat-treated at (a) 0Cr, 1150°C (b) 10Cr, 1150°C (c) 20Cr, 1150°C, (d) 0Cr, 1200°C, (e) 10Cr, 1200°C and (f) 20Cr, 1200°C.

In all of the above deconvoluted peaks for the alloy's solution treated at 1150°C and 1200°C followed by cooling under WQ in Fig. 4.19, AC in Fig. 4.20 and FC in Fig. 4.21, the  $\gamma'$  peak is considered to have lower diffraction angle due to higher lattice parameter than  $\gamma$ . (200) plane was chosen for deconvolution as  $\gamma'$  forms on (100) plane. The misfit calculated by the deviation in the d-spacing at (200) for all heat-treatment condition is represented in Table 4.2.

Table 4.2: The lattice misfit for all three solutionized alloys under various cooling mediums.

At.% Cr	Lattice misfit - 1150°C, WQ	Lattice misfit. 1200°C, WQ
0Cr	0.29	0.81
10Cr	0.34	0.64
20Cr	0.11	0.32
At.% Cr	Lattice misfit - 1150°C, AC	Lattice misfit. 1200°C, AC
0Cr	0.83	0.46
10Cr	0.42	0.44
20Cr	0.42	0.34
At.% Cr	Lattice misfit - 1150°C, FC	Lattice misfit. 1200°C, FC
0Cr	1.32	1.16
10Cr	1.22	1.06
20Cr	1.89	0.88

A comparison of the lattice mismatch between  $\gamma$  and  $\gamma'$  for the alloys heat-treated under various conditions is shown in Table 4.2. The lattice mismatch is calculated by the deviation in the d-spacing of the (200) deconvoluted peak, considering that  $\gamma'$  forms over the (100) plane. These plots reveal a positive lattice mismatch for all the three alloys and are not affected by the heat-treatment methods. A decreasing lattice mismatch with an increase in the Cr content for all three cooling rates is observed for the alloys cooled by 1150°C and 1200°C, indicating a crucial role of Cr that increases the lattice parameter of the  $\gamma$  phase.

A decrease in the lattice misfit is also observed when alloys are cooled from 1200°C compared to alloys cooled from 1150°C. This is observed when the alloys are cooled by AC and FC but not for WQ. Correlating the lattice misfit with the  $\gamma'$  particle size infers the dissolution of the  $\gamma'$  phase being efficient when the samples are cooled from 1200°C due to a decrease in the size compared to when cooled from 1150°C [22].

#### 4.7 Micro Hardness Measurements

The micro-hardness results taken at 500gf for the solutionized samples at 1150°C and 1200°C as shown in the Figure 4.22 relate to the SEM images in Fig. 4.13, Fig. 4.14 and Fig. 4.15. According to the FEG-SEM results and the  $\gamma'$  size distribution curves, it is observed that with a decrease in the cooling rates, coarsening of  $\gamma'$  is observed, resulting in an increase in hardness progressively from WQ to AC to FC.

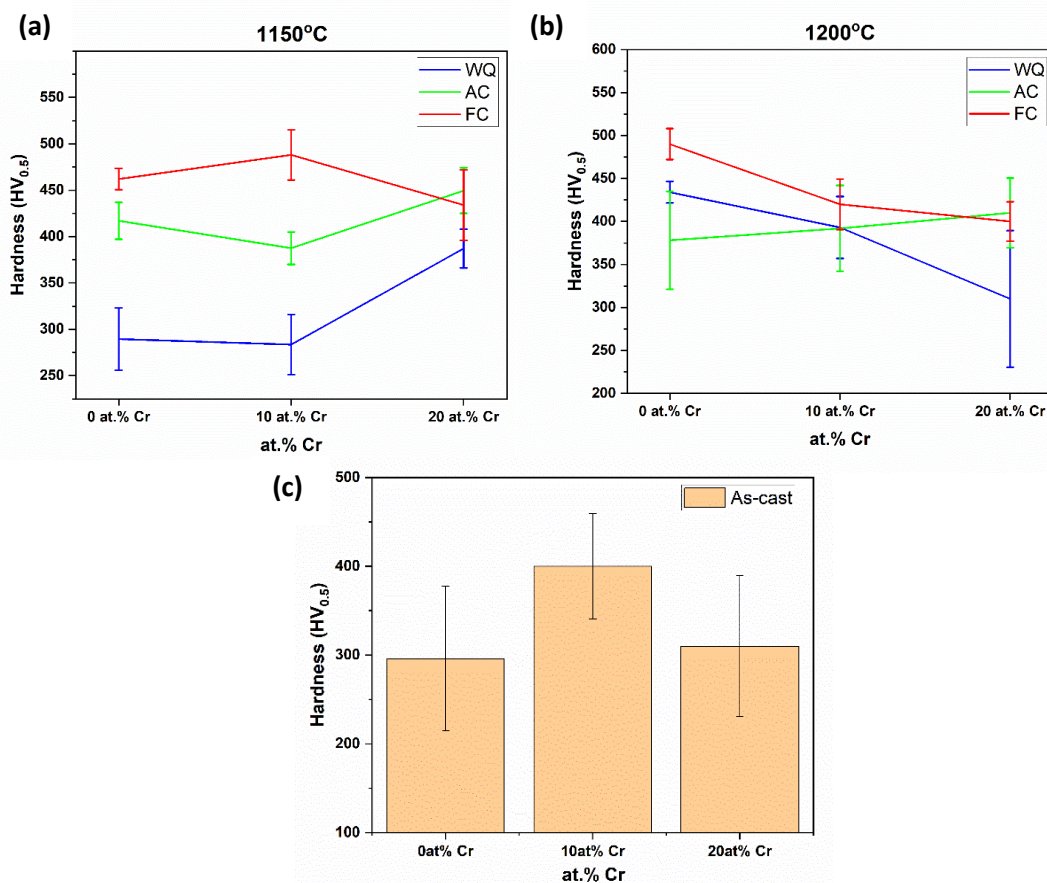


Fig. 4.22: Micro-hardness results of solutionized samples at (a) 1150°C and (b) 1200°C and (c) as-cast samples with increasing Cr content.

Hardness variation with Cr is seen in Figure 2.5 as reported by K.A. Christofidou et al. [14]. They have reported a decrease in the hardness with an increase in the Cr content. However, the results obtained in Figure 4.22 for alloys with 0at.%Cr, 10at.% Cr and 20at.% Cr show a dependence of the hardness on the heat treatment temperature. For 1150°C, the hardness values increase with increased Cr content for WQ and AC samples but decrease for FC samples. However, a decrease in the hardness values is observed for all heat-treated samples at 1200°C, while a negligible change is observed for samples cooled by air cooling.

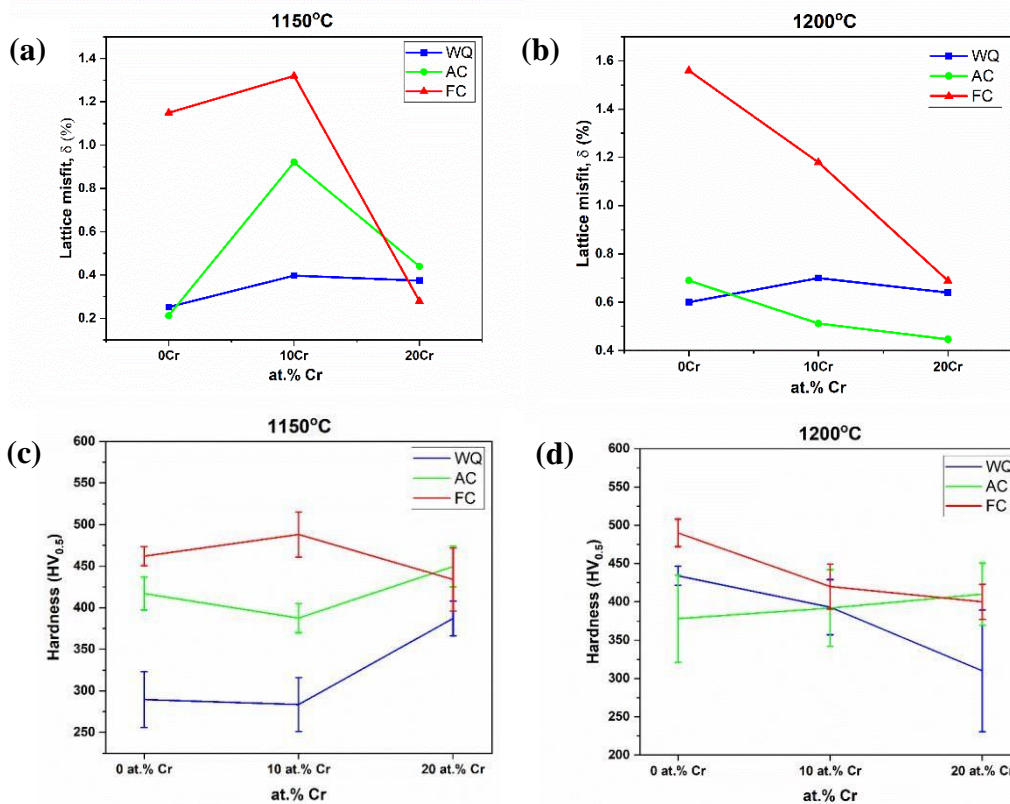


Fig. 4.23: Comparison of lattice misfit post solutionization at (a) 1150°C and (b) 1200°C with the hardness values post solutionization at (c) 1150°C and (d) 1200°C.

Figure 4.23 reveals a correlation of hardness values with the lattice misfit. The hardness values show a negligible change for FC alloys from 450HV to 430 HV with increasing %Cr from 0at.% Cr to 20at.% Cr when solutionized at 1150°C. This is seen in Figure 4.23 (a)-(c). Similar observations are made for the AC alloys where the hardness values change from 415HV to 440HV as Cr is increased from 0at.% Cr to 20at.% Cr. This correlated with a decreasing lattice misfit for AC and FC alloys as observed in Figure 4.23 (a).

Figure 4.23 (b)-(d) reveals a hardness and misfit comparison for the alloys heat-treated at 1200°C. Alloys having 0at.% Cr and solutionized at 1200°C shows higher hardness compared to alloys solutionized at 1150°C. This can be inferred to a higher volume fraction of  $\gamma'$  formed when cooled from 1200°C. A decreasing trend in the lattice misfit and hardness values is observed with increasing Cr percentage. Thus, it can be concluded that hardness values are related to the lattice mismatch in the material.

Understanding the behavior of the hardness wrt variation in the Cr content has to be thoroughly done by using advanced characterization tools like Atom Probe Tomography (APT) to understand the role of Cr in  $\gamma$  and  $\gamma'$  at different heat treatment temperatures.

#### 4.8 PROPERTY RELATION WITH VARYING at.% Cr

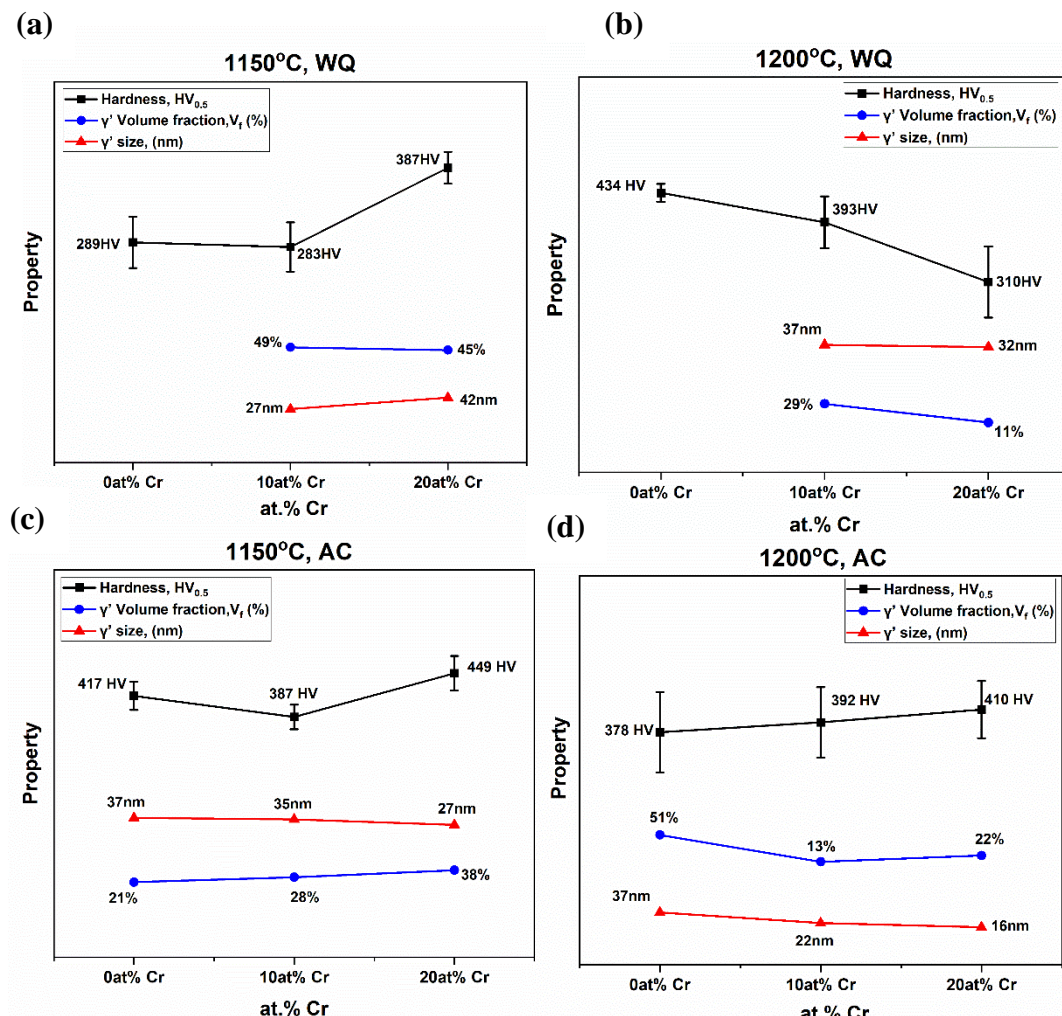


Fig. 4.24: Property relation of hardness,  $\gamma'$  volume fraction and  $\gamma'$  precipitate size wrt %Cr for alloys solutionized at (a) 1150°C, WQ, (b) 1200°C, WQ, (c) 1150°C, AC and (d) 1200°C, AC.

The property relation correlating the hardness, volume fraction and  $\gamma'$  precipitate size wrt to the varying Cr percentages is shown in the Figure 4.24. The proportionality between each property is represented by,

$$\tau \propto \frac{1}{r} \propto vf \propto \text{Hardness} \dots\dots (19)$$

For all the heat-treatment conditions, it can be concluded that the hardness is inversely proportional to the precipitate size while it is directly proportional to the  $\gamma'$  volume fraction yielding a higher shear strength required for the deformation due to the activation of Orowan looping mechanism of precipitate strengthening. This will yield in a higher strength in the material satisfied by the formula,

$$\tau_{\text{strong}} = \sqrt{\frac{\gamma_{APB} G f}{r}} \dots\dots (20)$$

where,

$\gamma_{APB}$  = Anti Phase Boundary Energy

G = Shear Modulus

r =  $\gamma'$  particle size

f =  $\gamma'$  volume fraction

Thus, it can be concluded that finer sized precipitates yield higher strength. However, for the alloys solutionized at 1150°C followed by WQ, the hardness show a direct relation with the  $\gamma'$  size and thus does not satisfy the high shear strength criteria shown in the equation 20.

## **Chapter 5**

### **CONCLUSIONS AND FUTURE SCOPE**

- I. It can be concluded that the complete dissolution of  $\gamma'$  takes place when solutionized for 48h at the super-solvus temperature but  $\gamma'$  forms as cooling precipitates due to faster kinetics of the  $\gamma'$  forming elements.
- II. Cr plays a key role in decreasing the  $\gamma/\gamma'$  lattice misfit, thereby influencing the shape of  $\gamma'$  transforming from cuboidal to spherical or rounded cubes.
- III. Effect of Cr on the  $\gamma'$  size shows a decreasing trend with increasing Cr content.
- IV. Primary  $\gamma'$  size is found to coarsen for furnace cooled alloys post solutionization both at 1150°C and 1200°C. This indicates a decrease in the volume fraction of secondary  $\gamma'$  in the FC condition as observed from the SEM images in Fig. 4.15 for the alloys solutionized at 1200°C.

#### **Future Scope**

- I. Aging studies can be done for the alloys solutionized at 1150°C and 1200°C followed by WQ.
- II. Aging curves can be plotted with precipitate size, volume fraction and hardness to optimize the Cr content added to the alloy as well as the aging time period.
- III. Behavior of the hardness wrt variation in the Cr content can be thoroughly investigated by using advanced characterization tools like Atom Probe Tomography (APT) to understand the partitioning of Cr in  $\gamma$  and  $\gamma'$  at different heat treatment temperatures.
- IV. High temperature mechanical properties like fatigue, creep, and high temperature yield strength can be studied after the aging treatment.

## REFERENCES

1. J. Sato T. Omori, K. Oikawa, R. Kainuma, K. Ishida, 'Cobalt-Base High-Temperature Alloys', Science 312, 90 (2006), pg. no: 90-91.
2. Rafael Casas Ferreras, 'Design of high temperature cobalt-based alloys processed by powder metallurgy route', Doctoral Thesis, University Carlos III de Madrid, (2018), pg. no: 22-24.
3. Surendra Kumar Makineni, Mahander Pratap Singh, Kamino Chattopadhyay, 'Annual Review of Materials Research Low-Density, High-Temperature Co Base Superalloys', Annual Rev. Mater. Res. (2021), pg. no: 187-208.
4. Agnieszka Tomaszewska, H. Eckerlebe, L. Karge, P. Staron, 'Primary microstructure, micro-segregation and precipitates characterization of an as-cast new type  $\gamma/\gamma'$  Co-Al-Mo-Nb cobalt-based superalloy', Journal of Alloys and Compounds 750 (2018), pg. no: 90-97.
5. SK. Makineni, A. Samanta, T. Rojhirunsakool, T. Alam, B. Nithin, A.K. Singh, R. Banerjee, K. Chattopadhyay, 'A new class of high-strength high-temperature Cobalt based  $\gamma/\gamma'$  Co–Mo–Al alloys stabilized with Ta addition', Acta Materialia 97 (2015), pg. no: 29-40.
6. Semanti Mukhopadhyaya, Prafull Pandey, Nithin Baler, Krishanu Biswas, Surendra Kumar Makineni, Kamino Chattopadhyay, 'The role of Ti addition on the evolution and stability of  $\gamma/\gamma'$  microstructure in a Co-30Ni-10Al-5Mo-2Ta alloy', Acta Materialia 208 (2021), pg. no: 35-48.
7. Subhashish Meher, 'Comparative coarsening kinetics of gamma prime precipitates in Nickel and Cobalt base superalloys', Dissertation for Doctorate of Philosophy, University of North Texas, (2014), pg. no: 121-126.
8. Tianyou Wang, Xiaomeng Wang, Zihua Zhao, Zheng Zhang, 'Dissolution behaviour of the  $\gamma'$  precipitates in two kinds of Ni-based superalloys', Materials at High Temperatures (2016), pg. no: 51-57.
9. N. El-Bagoury, M. Waly, A. Nofal, 'Effect of various heat treatment conditions on microstructure of cast polycrystalline IN738LC alloy', Materials Science and Engineering A 487 (2008), pg. no: 152-161

10. Mohammad Mehdi Barjesteh, Seyed Mehdi Abbasi, Karim Zangeneh Madar,’ The effect of heat treatment on characteristics of the gamma prime phase and hardness of the nickel-based superalloy Rene®80’, Materials Chemistry and Physics, (2019), pg. no: 46-55
11. H. R. Abedi, O. A. Ojo, Xinjin Cao,’ effect of cooling rate on precipitation behavior of gamma prime in a newly developed Co-based superalloy’, Process Design And Materials Development For High-Temperature Applications, (2020), pg. no: 22- 30.
12. Dao-Guang He, Y.C. Lin, Yi Tang, Ling Li, Jian Chen, Ming-Song Chen, Xiao-Min Chen, ‘Influences of solution cooling on microstructures, mechanical properties and hot corrosion resistance of a nickel-based superalloy’ Materials Science & Engineering A 746 (2019), pg. no: 372-383
13. Surendra K Makineni, ‘An Overview on Co-Base Alloys for High Temperature Applications’.
14. K.A. Christofidou, N.G. Jones, E.J. Pickering, R. Flacau, M.C. Hardy, H.J. Stone,’ The microstructure and hardness of Ni-Co-Al-Ti-Cr quinary alloys,’ Journal of Alloys and Compounds 688 (2016), pg. no: 542-552 .
15. Qiuzhi Gao, Yujiao Jiang, Ziyun Liu, Hailian Zhang, Chenchen Jiang,’ Effects of alloying elements on microstructure and mechanical properties of Co-Ni-Al-Ti superalloy’, Materials Science & Engineering A 779 (2020), pg. no: 51-61.
16. Hael Mughrabi,’ The importance of sign and magnitude of  $\gamma/\gamma'$  lattice misfit in superalloys – with special reference to the new  $\gamma'$ -hardened cobalt-base superalloys’, Acta Materialia, Volume 81, (2014), pg. no: 21-29.
17. Xingjun Liu, Wensu Cai, Zhongfeng Chen, Yuechao Chen, Xin Chen, Shuiyuan Yang, Yong Lu, Jiajia Han, Cuiping Wang, ’Effects of alloying additions on the microstructure, lattice misfit and solvus temperature of a novel Co-Ni based superalloy’, Intermetallics, Volume 141, (2022), pg. no: 1-10.
18. Guochao Huang et al., ‘The effect of cooling rates from temperatures above the  $\gamma'$  solvus on the microstructure of a new nickel-based powder metallurgy superalloy’ Journal of Alloys and Compounds 747 (2018) pg. no: 1062 – 1072.
19. R.W. Kozer, A. Suzuki, W.W. Milligan, J.J. Schirra, M.F. Savage, T.M. Pollock ‘Strengthening mechanisms in polycrystalline multimodal nickel-base superalloys, Metallurgical and Materials Transaction, A (2009), pg. no: 1588 – 1603.
20. D. Raynor, J.M. Silcock, ‘Strengthening mechanisms in  $\gamma'$  precipitating alloys’, Metal Sci. 4 (1970), pg. no: 121 -130.

21. Shaik Adil, M.V. Suraj, Lava Kumar Pillari, Soumya Sridar, M. Nagini, K.G. Pradeep, B.S. Murty, ‘On the effect of Fe in L12 strengthened Al-Co-Cr-Fe-Ni-Ti complex concentrated alloy, Materialia 14 (2020), pg. no: 135-145.
22. Liang Luo, Cheng Ai, Yue Ma, Shusuo Li, Yanling Pei, Shengkai Gong, ‘Influence of temperature on the lattice misfit and elastic moduli of a Ni based single crystal superalloy with high volume fraction of  $\gamma'$  phase’ Materials Characterization 142 (2018), pg. no: 27-38.